

On the properties of X-ray corona in Seyfert 1 galaxies

INDRANI PAL ^{1,2,3} ANJU A.,⁴ H. SREEHARI,^{1,5} GITIKA RAMESHAN,⁶ C. S. STALIN,¹ CLAUDIO RICCI,^{7,8} AND
S. MARCHESI ^{9,3,10}

¹Indian Institute of Astrophysics, Bangalore, 560034, Karnataka, India

²Pondicherry University, R.V. Nagar, Kalapet, 605014, Puducherry, India

³Department of Physics and Astronomy, Clemson University, Kinard Lab of Physics, Clemson, SC 29634, USA

⁴Department of Physical Sciences, Indian Institute of Science Education And Research Kolkata, Mohanpur, Nadia-741246, West Bengal, India

⁵Department of Physics, Faculty of Natural Sciences, University of Haifa, Mount Carmel, Haifa 3498838, Israel

⁶Cochin University of Science and Technology, South Kalamassery, Kochi, Kerala, 682022, India

⁷Instituto de Estudios Astrofísicos, Facultad de Ingeniería y Ciencias, Universidad Diego Portales, Avenida Ejercito Libertador 441, Santiago, Chile

⁸Kaoli Institute for Astronomy and Astrophysics, Peking University, Beijing 100871, China

⁹Dipartimento di Fisica e Astronomia (DIFA), Università di Bologna, via Gobetti 93/2, I-40129 Bologna, Italy

¹⁰INAF - Osservatorio di Astrofisica e Scienza dello Spazio di Bologna, Via Piero Gobetti, 93/3, 40129, Bologna, Italy

Abstract

We carried out a uniform and systematic analysis of a sample of 112 nearby bright Seyfert 1 type AGN, the observations of which were carried out by the *Nuclear Spectroscopic Telescope Array (NuSTAR)* between August 2013 and May 2022. The main goal of this analysis is to investigate the nature of the X-ray corona in Seyfert 1 galaxies. By fitting a physical model to the *NuSTAR* spectra, we were able to constrain the high-energy cut-off (E_{cut}) for 73 sources in our sample. To estimate the temperature of the corona (kT_e) in our sample of 112 sources, we used the Comptonization model to fit their spectra. We could constrain kT_e in 42 sources. We found a strong positive correlation between E_{cut} and kT_e with most of the sources lying above the empirical approximation of $E_{\text{cut}} = 2-3 kT_e$. We investigated for possible correlations between various properties of the corona obtained from physical model fits to the observed spectra and between various coronal parameters and physical properties of the sources such as Eddington ratio and black hole mass. We found (a) a strong correlation between E_{cut} and the photon index and (b) a significant negative correlation between kT_e and the optical depth. From detailed statistical analysis of the correlation of coronal parameters with the Eddington ratio and black hole mass, we found no significant correlation. The correlations observed in this study indicate that an optically thin corona is needed to sustain a hotter corona with a steeper spectrum.

Keywords: galaxies: active — galaxies: nuclei — galaxies: Seyfert — X-rays: galaxies

1. INTRODUCTION

Most massive galaxies host supermassive black holes (SMBHs) at their centres with masses (M_{BH}) of the order of 10^5 to $10^{10} M_{\odot}$. These SMBHs power active galactic nuclei (AGN) by accretion of matter from their surroundings (Salpeter 1964; Lynden-Bell 1969; Shakura & Sunyaev 1973; Guilbert et al. 1983; Ho 2008). The observed optical, ultra-violet (UV) radiation from these accretion-powered systems is believed to be thermal emission from the standard optically thick, geometrically thin accretion disk (Shields 1978; Malkan & Sargent 1982; Sun & Malkan 1989) that surrounds the SMBHs. These AGN are also sources of intense X-ray

emission (Elvis et al. 1978; Mushotzky et al. 1993). The X-ray emission in the radio-quiet category of AGN is believed to originate from a compact region that contains hot electrons ($T_e \sim 10^{8-9} K$) called the corona situated close to the vicinity of the SMBH. Observations indicate that the corona is physically compact with size scales of the order of $3 - 10 R_G$ (McHardy et al. 2005; Risaliti et al. 2005), where R_G is the gravitational radius defined as $R_G = GM_{BH}/c^2$, here, G is the gravitational constant and c is the speed of light. The hot electrons in the corona, inverse Compton scatter the optical or UV thermal photons from the geometrically thin, optically thick accretion disk, thereby producing X-ray emission

(Haardt & Maraschi 1991, 1993). The emergent X-ray spectrum follows a power law with the high energy roll off of the form $N(E) \propto E^{-\Gamma} \exp(-E/E_{\text{cut}})$, where Γ is the power law photon index and E_{cut} is the high energy cut-off (Sunyaev & Titarchuk 1980). In this paradigm, expecting a connection between the accretion disk and the X-ray-emitting corona is natural. One piece of observational evidence for this accretion disk corona connection is the observed positive correlation (Shemmer et al. 2008; Risaliti et al. 2009; Jin et al. 2012; Liu et al. 2021; Tortosa et al. 2022a) between Γ and the mass-normalized accretion rate usually represented by the Eddington ratio ($\lambda_{\text{Edd}} = L_{\text{Bol}}/L_{\text{Edd}}$). Here, L_{Bol} is the bolometric luminosity and L_{Edd} is the Eddington luminosity defined as $L_{\text{Edd}} = 1.3 \times 10^{38} M_{\text{BH}}/M_{\odot} \text{ erg s}^{-1}$. A possible explanation for this observed correlation is that at a higher λ_{Edd} the increased optical, UV photons from the accretion disk can lead to a more effective cooling of the corona, thereby leading to a decrease in the temperature of the corona (kT_e) and larger Γ or softening of the X-ray spectrum. Recently, Ricci et al. (2018) proposed that another explanation for this is the pair thermostat, due to the changes in temperature across the compactness–temperature ($l - \theta$) plane, and they could successfully reproduce the slope of the $\Gamma - \lambda_{\text{Edd}}$ correlation.

According to Comptonization models, for a corona with slab geometry, E_{cut} is related to the temperature of the corona as $E_{\text{cut}} = 2-3 kT_e$ for optically thin and thick plasma respectively (Petrucci et al. 2001). However, according to Liu et al. (2014), the relation between E_{cut} and kT_e cannot be simple in the case of the non-static corona. Also, Middei et al. (2019) have shown that the relation of $E_{\text{cut}} = 2-3 kT_e$ is only valid for low values of kT_e and τ . Recently, for the source MR 2251–178, Pal et al. (2022) found $E_{\text{cut}} = 4.84 \pm 0.11 kT_e$, which deviates from the generally considered relation between E_{cut} and kT_e (Petrucci et al. 2001). Also, Γ is expected to depend on various parameters of the corona, such as its temperature kT_e , the optical depth (τ) as well as the seed photon temperature. To understand the properties of AGN, it is important to have better constraints on the coronal parameters of AGN that characterise the X-ray emission, such as Γ and kT_e .

Earlier studies on the determination of the temperature of the corona in Seyfert galaxies used data from high-energy instruments such as the CGRO (Zdziarski et al. 2000; Johnson et al. 1997), *BeppoSAX* (Nicastro et al. 2000; Dadina, M. 2007), *INTEGRAL* (Malizia et al. 2014; Lubiński et al. 2010, 2016), *Swift-BAT* (Vasudevan et al. 2013; Ricci et al. 2017; Ricci et al. 2018) and *Suzaku* (Tazaki et al. 2011). These studies

have found that in Seyfert galaxies, the coronal temperature shows a wide range, with the values of E_{cut} ranging from 50–500 keV. These less sensitive observations were, however, limited to nearby bright Seyfert galaxies. Increased interest in studies on the hard X-ray spectra of AGN, as well as the determination of its coronal temperature, happened after the launch of the *Nuclear Spectroscopic Telescope Array* (*NuSTAR*; Harrison et al. 2013) in the year 2012, due to its wide spectral coverage of 3–79 keV and its high sensitivity beyond 10 keV. Since its launch, values of the temperature of the corona are known for many AGN, but most of those studies are restricted to the determination of E_{cut} . Also, data from *NuSTAR* have led to the finding of the variation in kT_e (Barua et al. 2020, 2021; Kang et al. 2021; Pal et al. 2022; Pal & Stalin 2023) as well as E_{cut} (Zoghbi et al. 2017; Ballantyne et al. 2014; Ursini et al. 2016; Ursini, F. et al. 2015; Keek & Ballantyne 2016; Zhang et al. 2018; Kang et al. 2021).

In recent years, there have been a few studies on characterising the temperature of the corona (E_{cut} or kT_e) in samples of AGN (Kamraj et al. 2018; Tortosa, A. et al. 2018; Molina et al. 2019; Rani et al. 2019; Baloković et al. 2020; Panagiotou & Walter 2020; Kang et al. 2020; Hinkle & Mushotzky 2021; Akylas, A. & Georgantopoulos, I. 2021; Kamraj et al. 2022; Kang & Wang 2022; Pal & Stalin 2023). Most of these studies focused on the determination of E_{cut} from phenomenological model fits to the observed X-ray spectra. Though E_{cut} can serve as a good proxy for kT_e , the recent findings of deviation from the $E_{\text{cut}} = 2-3 kT_e$ in few sources, have necessitated the determination of kT_e in AGN based on physical model fit to the observed X-ray spectra. The literature also contains results on E_{cut}/kT_e values and their correlation with other physical parameters. However, these correlations vary between studies, possibly due to small sample sizes and large error bars in the E_{cut}/kT_e measurements. Therefore, it is crucial to increase the sample size, analyze data consistently, and explore various correlations. To address these, we carefully selected type 1 sources with good signal-to-noise spectra from the *NuSTAR* archive and homogeneously conducted the needed analysis with a larger sample size than before.

In this work, we carried out an analysis of 112 Seyfert 1 type AGN to determine E_{cut} based on physical model fits to the *NuSTAR* data. Of these 112 sources, we could constrain E_{cut} in 73 sources. Further, physical model fits were carried out on the 112 sources to constrain kT_e . We could constrain kT_e in 42 sources. We investigated the correlation between different physical parameters obtained from the physical model fits. The

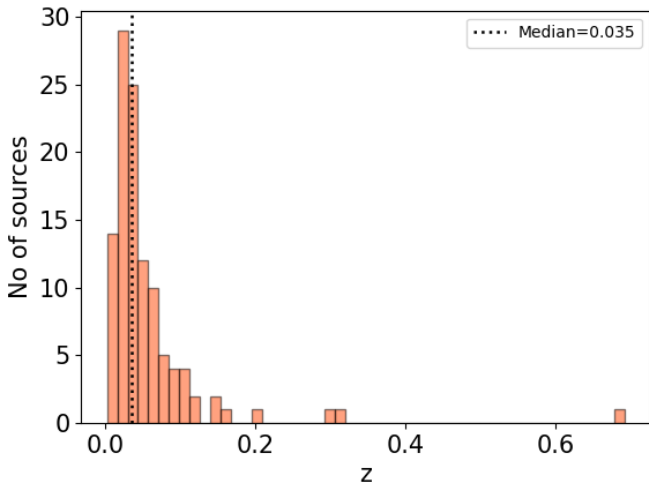


Figure 1. The redshift distribution of the sources. The vertical dotted line is the median of the distribution ($z=0.035$).

selection of our sample of sources and data reduction are given in Section 2. We describe in Section 3 the model fits carried out on the data; the results are given in Sections 4 and 5, and a comparison of our findings on E_{cut} and kT_e with those found from the literature are given in Section 6, followed by the discussion and the summary in the final two sections. In this work we adopted the cosmological parameters of $H_0 = 70 \text{ km sec}^{-1} \text{ Mpc}^{-1}$, $\Omega_M = 0.3$ and $\Omega_\lambda = 0.7$. All the quoted uncertainties in the derived parameters were calculated at the 90 per cent confidence level.

2. SAMPLE SELECTION AND DATA REDUCTION

2.1. Sample selection

Our sample of sources for this study was selected from the *NuSTAR* Master Catalog¹. We examined publicly accessible data for Seyfert galaxies sourced either from the *Swift-BAT* 105-month catalogue (Oh et al. 2018) or from the NASA/IPAC Extragalactic Database (NED) during the period spanning August 2013 to May 2022. We found a total of 850 Seyfert galaxies. We selected only Seyfert 1 galaxies with a net count rate greater than 0.1 counts/sec in the 3–79 keV band to have a sufficiently good signal-to-noise ratio spectrum for model fitting. Adopting the above-mentioned criteria, we arrived at a final sample of 130 Seyfert 1 galaxies spanning the redshift interval of $0.002 < z < 0.692$. Of these 130 sources, around 90 per cent of the sources were studied in Ricci et al. (2017). Ricci et al. (2017) carried out

the broadband (0.3–150 keV) X-ray spectroscopic analysis of *Swift-BAT* selected sources by combining *XMM-Newton*, *Swift/XRT*, *ASCA*, *Chandra*, and *Suzaku* observations in the soft X-ray band with 70-month averaged *Swift/BAT* data. Based on the value of the line of sight column densities (N_H) required in the absorption power law fit, 18 sources were classified as obscured AGN ($10^{22} \leq (N_H \text{ cm}^{-2}) < 10^{24}$) in Ricci et al. (2017). For this study, we selected the 112 unobscured nearby AGN with a median redshift of 0.035. We show in Fig. 1 the redshift distribution for our sample of sources. The redshifts are taken from SIMBAD². The full list of the Seyfert 1 galaxies and their *NuSTAR* observational details are given in Table 2. Among 112, about 50% of sources were observed more than once by *NuSTAR*. The observations with the highest exposure were chosen for this study to ensure good signal-to-noise ratio spectra.

2.2. Data reduction

For the 112 sources, we carried out the reduction of the raw event data taken from the HEASARC archive³, using the standard *NuSTAR* data reduction software NuSTARDAS⁴ v1.9.3 distributed by HEASARC within HEASoft v6.26.1. We generated the calibrated and cleaned event files using the `nupipeline` task and the instrument responses taken from the *NuSTAR* calibration database (CALDB release 20190607). To exclude the periods of elevated background, we selected the filtering options SAACALC=2, SAAMODE=OPTIMIZED and TENTACLE=YES to consider the passage of the satellite through the South Atlantic Anomaly (SAA). The source regions for the 112 Seyferts were extracted using circular radii between $30'' - 70''$ to maximize the S/N, depending on the source. A source-free circular area of the same radius on the same chip was selected to extract the background counts. All the science products, including energy spectra, response matrix files (RMFs) and auxiliary response files (ARFs), were generated using the task `nuproducts` for both the focal plane modules FPMA and FPMB. For spectral analysis, we fitted the background subtracted spectra from FPMA and FPMB simultaneously using XSPEC version 12.10.1 (Arnaud 1996), allowing the cross normalization factor to vary freely during spectral fits. The spectra were binned to have minimum counts of 20 per spectral energy bin. We note that, for faint sources, the binning of 20 counts/bin could be insufficient at the high energy end with $E > 50$

² <http://simbad.cds.unistra.fr/simbad/>

³ <https://heasarc.gsfc.nasa.gov/db-perl/W3Browse/w3browse.pl>

⁴ https://heasarc.gsfc.nasa.gov/docs/nustar/analysis/nustar_swgguide.pdf

¹ <https://heasarc.gsfc.nasa.gov/W3Browse/nustar/numaster.html>

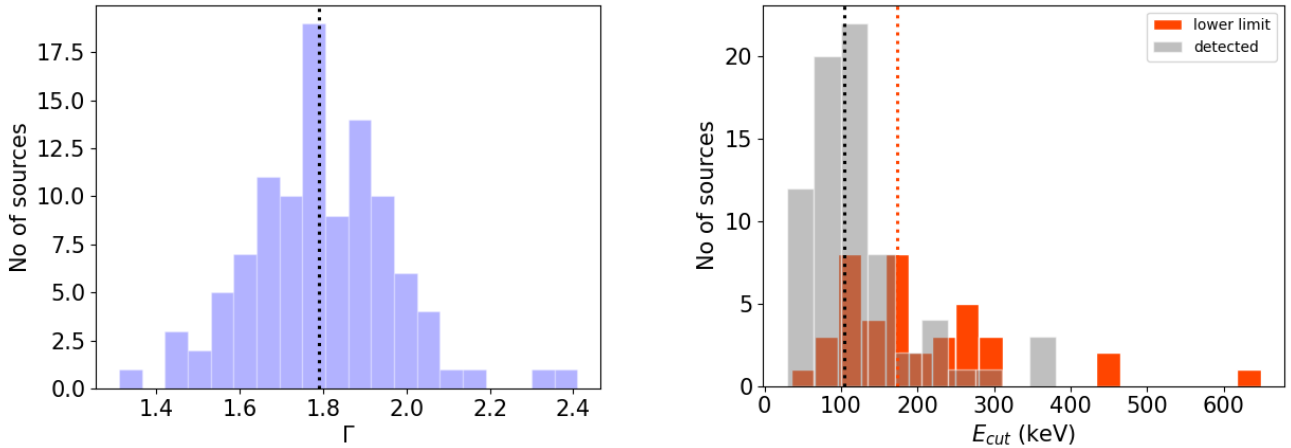


Figure 2. Distribution of Γ (left panel) and distribution of E_{cut} (right panel) obtained from Model–1 fit to all 112 source spectra. The vertical dotted lines are the median of the distributions.

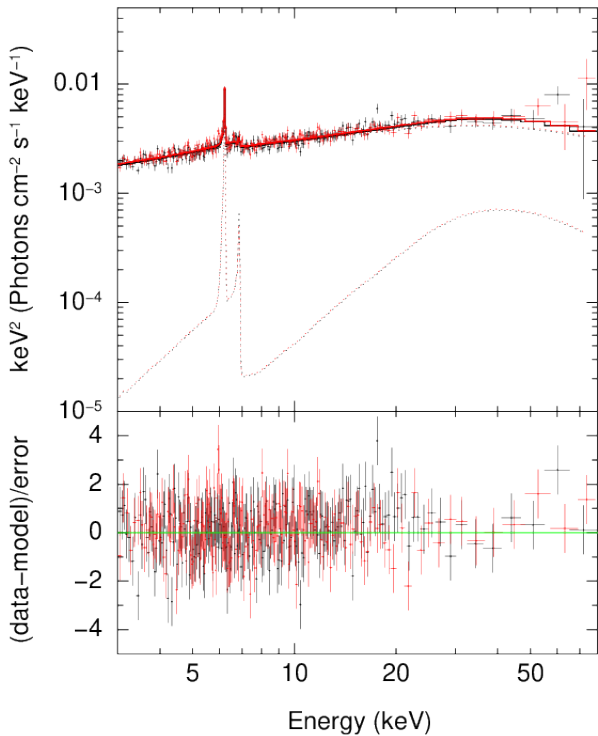


Figure 3. The best-fit unfolded FPMA/FPMB spectra of Mrk 279 (upper panel) with data to model residue of the Model–1c fit to the source spectra (lower panel).

keV for the χ^2 statistics to be applicable. Also, it is likely that the choice of binning can have some effect on the derived E_{cut} or kT_e values. To verify this, we identified the 10 faintest sources in our sample and redid the analysis using a binning of 50 counts/bin. For those faint sources, we found that the E_{cut} values obtained using a binning of 50 counts/bin agree within errors to

those obtained with a binning of 20 counts/bin. Therefore, it is likely that the binning choice adopted in this work has a negligible effect on the derived values of E_{cut} and/or kT_e . To get an estimate of the model parameters that best describe the observed data, we used the chi-square (χ^2) statistics, and for calculating the errors in the model parameters, we used the $\chi^2 = 2.71$ criterion, which is equivalent to the 90 per cent confidence range in XSPEC.

3. SPECTRAL ANALYSIS

We carried out a detailed spectral analysis of the *NuSTAR* data in the energy range of 3–79 keV for the 112 sources, a few of which also have soft X-ray observations. Since these are unobscured Seyfert 1 galaxies, we do not have degeneracies between N_{H} and continuum parameters that have been found in obscured Seyfert 2 galaxies (Marchesi et al. 2018). Therefore, we chose to fit the *NuSTAR* data alone, and we do not expect our results to be significantly affected by the lack of information at energies < 3 keV. In the past, too, a similar approach has been followed in several studies (Tortosa, A. et al. 2018; Kamraj et al. 2018; Baloković et al. 2020; Ezhikode et al. 2020; Kang et al. 2020; Akylas, A. & Georgantopoulos, I. 2021) aimed at characterising the corona. For the completeness of our study, we compared our findings with those found in the literature where E_{cut}/kT_e were obtained with and without the soft X-ray coverage (see Table 3).

We used the following two models

- Model–1: $\text{CONST} \times \text{TBABS} \times \text{zTBABS} \times (\text{XILLVER}/\text{RELXILL}/(\text{RELXILL}+\text{XILLVER}))$
- Model–2: $\text{CONST} \times \text{TBABS} \times \text{zTBABS} \times (\text{XILLVERCP}/\text{RELXILLCP}/(\text{RELXILLCP}+\text{XILLVERCP}))$

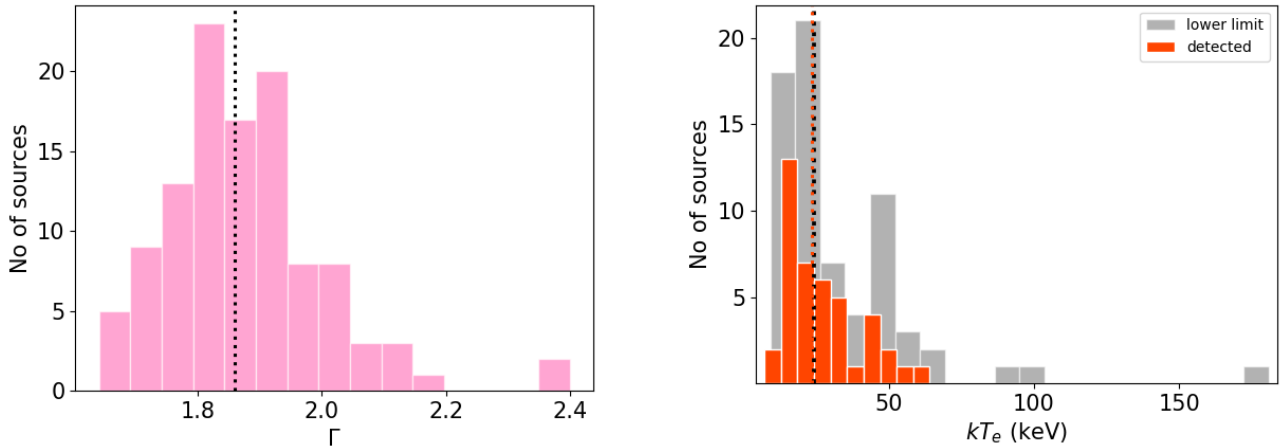


Figure 4. Distribution of Γ (left panel) and kT_e (right panel) from Model–2 fit for 112 sources. The vertical dotted lines are the median of the distributions.

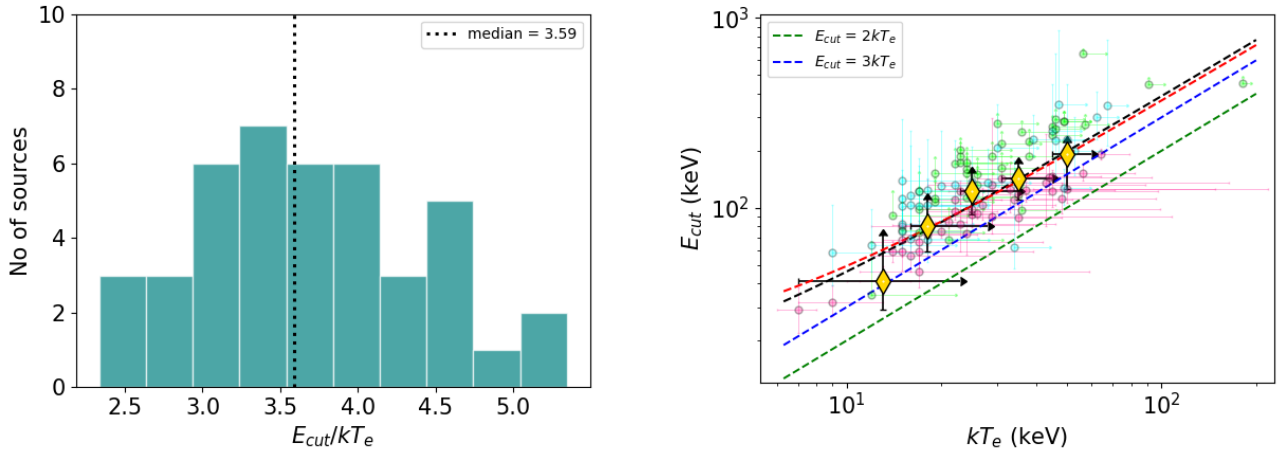


Figure 5. Distribution of the ratio between E_{cut} to kT_e for the 42 sources with kT_e measurements (left panel). The vertical dot line is the median of the ratio. The variation of E_{cut} against kT_e (right panel). Here, the green dashed line shows the $E_{\text{cut}} = 2kT_e$ relation, the blue dashed line shows the $E_{\text{cut}} = 3kT_e$ relation. The black dashed line is the linear least squares fit to the median values of E_{cut} (yellow diamond points) obtained from the KMPL survival analysis in each kT_e bins. The best fit is $E_{\text{cut}} = (3.80 \pm 0.53)kT_e + (8.15 \pm 16.51)$. The red dashed line is the linear relation obtained from the statistical analysis package *ASURV*. The pink dots with error bars are the constrained values, and the green dots represent the censored values of E_{cut} and kT_e ; the cyan dots denote the constrained values of E_{cut} and lower limits of kT_e .

In both models, the Fe- $K\alpha$ line present in the source spectrum would be self-consistently taken care of. From our previous study (Pal et al. 2022; Pal & Stalin 2023), we confirmed that the model parameters such as, $E_{\text{cut}}/kT_e/R$, obtained using these models did not differ significantly from the best-fit measurements found from fitting the spectra with a phenomenological power law with a cut-off in which the Fe- $K\alpha$ line is not coupled with the reflection continuum.

In our both Model–1 and Model–2, CONST represents the calibration constant between the *NuSTAR* fo-

cal plane modules, FPMA and FPMB. TBABS was used to model the Milky Way Galactic hydrogen column density, which was taken from Willingale et al. (2013) for each source. The component zTBABS represents the hydrogen column density ($N_{\text{H}}^{\text{INT}}$) of the host galaxy. During the modelling of the source spectrum, the value of $N_{\text{H}}^{\text{INT}}$ was allowed to vary freely.

XILLVER/RELXILL (García & Kallman 2010; García et al. 2011) was used to model the spectra with an absorbed cut-off power law along with the reflection fea-

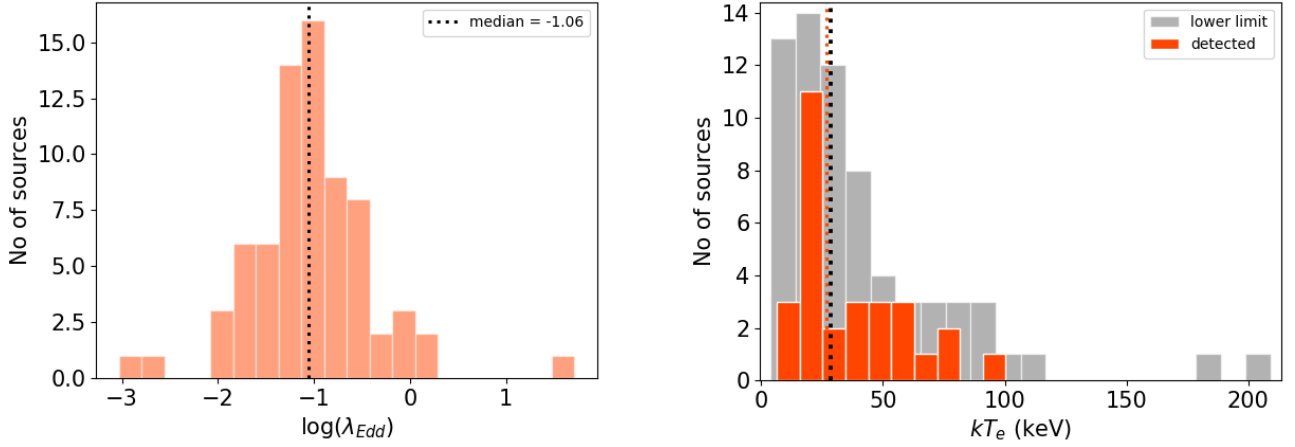


Figure 6. Left panel: Eddington ratio distribution for the 109 sources for which we could find the black hole mass from the literature. Right panel: Distribution of both constrained and censored values of kT_e as calculated using Equation 1 from the E_{cut} values taken from Ricci et al. (2018) for 96 sources which are common between this work and Ricci et al. (2018). The vertical dotted lines are the median of the distributions.

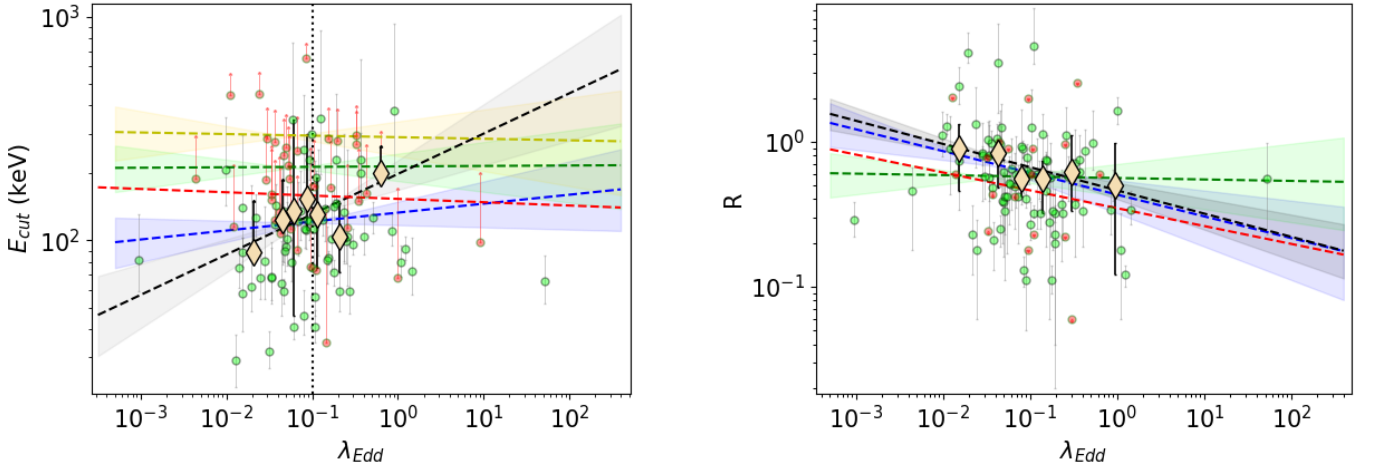


Figure 7. The relation between $E_{\text{cut}}-\lambda_{\text{Edd}}$ (left panel) and $R-\lambda_{\text{Edd}}$ (right panel). In the plots, the green dots denote the constrained values, and the red dots represent the lower/upper limits of the dependent parameters. In each panel, the blue dashed line is the linear fit to the constrained values, and the blue-shaded region indicates the errors in the slope and the intercept to the linear fit (Method I). The beige diamond points represent the median values of E_{cut} and R in each bin of λ_{Edd} obtained from the survival analysis using the KMPL approach. The black dashed line and the black shaded region are the linear fit and the errors in the fit parameters to the median values (Method II). The red dashed line represents the linear fit using the Schmitt method obtained using the package *ASURV*.

The green dashed line and the shaded region represent the linear fit and the errors in the slope and the intercept for the linear relation fit between two parameters considering both uncensored (including the corresponding asymmetric errors) and censored (upper bound of $E_{\text{cut}} = 500$ keV; lower bound of $R = 0.01$) values (Method III) in each panel. The yellow dashed line and the shaded region in the first panel are the linear fit, and the errors in the fit parameters are similar to the green shaded region but considering the upper bound of E_{cut} to be 1000 keV (Method IV).

tures present in it. In XSPEC Model–1 took the following forms,

- Model–1a: $\text{CONST} \times \text{TBABS} \times \text{zTBABS} \times (\text{XILLVER})$
- Model–1b: $\text{CONST} \times \text{TBABS} \times \text{zTBABS} \times (\text{RELXILL})$
- Model–1c: $\text{CONST} \times \text{TBABS} \times \text{zTBABS} \times (\text{RELXILL}+\text{XILLVER})$

During the fit using Model–1a, the parameters that were kept free were Γ , E_{cut} , R and the normalization (N_{xillver}) of the XILLVER component. The reflector was considered neutral; therefore, we fixed the ionization parameter ($\log\xi$) to 0.0. The values of AF_e and the inclination angle were fixed to the solar value ($=1.0$) and 30° respectively.

In Model–1b, we replaced XILLVER with RELXILL to take care of the relativistic smeared Comptonization spectrum for a few sources. In addition to the parameters described in Model–1a, there are a few more parameters, such as the inner and outer emissivity indices (β_1 and β_2 respectively), inner and outer radii of the accretion disk (r_{in} and r_{out} respectively), break radius (r_{br}) between r_{in} and r_{out} and the spin of the black-hole (a_*). We tied β_1 and β_2 together during the fit and kept them as free parameters. r_{br} , r_{in} and r_{out} were kept frozen to their default values of $15r_g$, $3r_g$ and $400r_g$ respectively. We considered a highly spinning SMBH and fixed a_* to 0.998 (Thorne 1974). AF_e was frozen to the solar value. The inclination angle was fixed to 30° . The other parameters that were kept free during the fit were Γ , E_{cut} , R , $\log\xi$ and the normalization (N_{relxill}) of the RELXILL model.

The spectra of a few sources could not be well-fitted using either XILLVER or RELXILL. In those sources, where significant narrow Fe-K α emission lines were detected, we used Model–1c, in which we fitted RELXILL and XILLVER together. Between these two components Γ , kT_e and AF_e were tied together and kept as free parameters during the fitting. The other parameters were treated similarly as described earlier in Model–1a and Model–1b. We could constrain E_{cut} for 73 sources from the model fits. The summary of the spectral analysis from this model fits to the spectra given in Table 3.

Out of 112 sources, we used Model–1a in 86 sources to estimate different coronal parameters. In 20 out of the remaining 26 Seyferts, the presence of a broad emission line was confirmed. To take care of the relativistic broadening of the Fe-K α line, we fitted the spectra of those sources with Model–1b. In the other six sources (ARK 564, MCG-06-30-15, Mrk 1044, Mrk 279, NGC

3783 and NGC 4051), we used a XILLVER component in addition to RELXILL (Model–1c), since one model alone could not fit the reflection spectra properly. The distributions of Γ and E_{cut} as found from the Model–1 fits are given in Fig. 2. The median value of Γ as obtained from the analysis using Model–1 was found to 1.79 ± 0.02 , which is consistent with the median value of Γ as found from the broad-band analysis of the unobscured sources by Ricci et al. (2017). Using only the constrained E_{cut} , a median of 104 ± 8 keV was obtained. The errors on the median values represent the statistical uncertainties, calculated as the standard deviation of the distribution divided by the square root of the sample size (σ/\sqrt{N} , where N is the number of data points). The broad-band spectral fit using Model–1c with the data to model residue for the source Mrk 279 is presented in Fig. 3.

We carried out the Comptonization model fits (Model–2) to the 112 sources to estimate the coronal temperature. We could constrain kT_e for 42 sources using this model. In XSPEC Model–2 took the following forms,

- Model–2a: $\text{CONST} \times \text{TBABS} \times \text{zTBABS} \times (\text{XILLVERCP})$
- Model–2b: $\text{CONST} \times \text{TBABS} \times \text{zTBABS} \times (\text{RELXILLCP})$
- Model–2c: $\text{CONST} \times \text{TBABS} \times \text{zTBABS} \times (\text{RELXILLCP}+\text{XILLVERCP})$

All the model parameters were handled similarly as described for Model–1. The best-fit values of various coronal parameters found from the Comptonization model fit (Model–2) are given in Table 4. The distribution of the best-fit values of Γ and kT_e , as obtained from Model–2, are shown in Fig. 4. The median value of Γ was determined to be 1.86 ± 0.01 , and when considering only the constrained value of kT_e , the median was found to be 24 ± 2 keV.

4. RELATION BETWEEN E_{CUT} AND kT_e

It is believed that the phenomenological high-energy cut-off could be related to the temperature as $E_{\text{cut}} = 2-3 kT_e$ (Petrucci et al. 2001). However, recent studies do indicate that this simple relation between E_{cut} and kT_e may not be valid for all sources (Liu et al. 2014; Middei et al. 2019; Pal et al. 2022). The relation can be complicated in the case of a non-static corona, such as the one with outflows (Liu et al. 2014). Also, according to Middei et al. (2019), the relation of $E_{\text{cut}} = 2-3 kT_e$

Table 1. Results of the correlation analysis between different parameters. Provided are the Spearman’s rank correlation coefficient (ρ) and the probability (p) for the null hypothesis (no correlation). We fail to reject the null hypothesis if p is larger than 0.01. Here, Method I indicates the correlation study between two parameters with only uncensored values. Method IIa represents the correlation analysis performed between the median values of two parameters obtained from the survival analysis method using the non-parametric KMPL approach. Method IIb is the bivariate correlation analysis performed using the package *ASURV*. The correlation analysis between two parameters considering both uncensored (including the corresponding asymmetric errors) and censored values ($E_{\text{cut}}^{\text{MAX}} = 1000$ keV, $R^{\text{MIN}} = 0.01$ and $kT_e^{\text{MAX}} = 150$ keV) is denoted by Method III, wherein Method IV represents the same as Method III except the $E_{\text{cut}}^{\text{MAX}}$ is considered to be 500 keV here.

Parameter 1	Parameter 2	Method	Full sample		Moderately accreting sources		Highly accreting sources	
			ρ	p	ρ	p	ρ	p
E_{cut}	λ_{Edd}	I	0.19	0.12	0.41	0.009	-0.02	0.89
		IIa	0.54	0.22	–	–	–	–
		IIb	0.06	0.55	0.11	0.39	-0.16	0.30
		III	0.03	0.75	0.12	0.37	-0.08	0.59
		IV	0.03	0.73	0.09	0.48	-0.08	0.61
R	λ_{Edd}	I	-0.28	0.01	-0.30	0.04	-0.07	0.68
		IIa	-0.25	0.05	–	–	–	–
		IIb	-0.22	0.02	-0.25	-0.06	-0.02	-0.88
		III	-0.18	0.07	-0.21	0.11	-0.002	0.73
R	Γ	I	0.28	0.009	–	–	–	–
		IIa	-0.55	0.26	–	–	–	–
		IIb	0.59	0.03	–	–	–	–
		III	0.30	0.002	–	–	–	–
E_{cut}	R	I	-0.03	0.84	–	–	–	–
		IIa	0.10	0.87	–	–	–	–
		IIb	0.18	0.08	–	–	–	–
		III	0.15	0.12	–	–	–	–
		IV	0.15	0.12	–	–	–	–
Γ	λ_{Edd}	I	0.17	0.08	0.18	0.16	0.1	0.49
		IIa	–	–	–	–	–	–
		IIb	–	–	–	–	–	–
		III	0.17	0.08	0.17	0.18	0.12	0.41
E_{cut}	Γ	I	0.69	1.75E-11	–	–	–	–
		IIa	0.99	1.46E-05	–	–	–	–
		IIb	0.57	0	–	–	–	–
		III	0.60	4.11E-12	–	–	–	–
		IV	0.61	1.75E-12	–	–	–	–
τ	kT_e	I	-0.96	1.82E-23	–	–	–	–
		IIa	-0.99	1.40E-24	–	–	–	–
		IIb	–	–	–	–	–	–
		III	-0.66	1.89E-10	–	–	–	–
E_{cut}	$\frac{M_{\text{BH}}}{M_{\text{Sun}}}$	I	-0.02	0.86	–	–	–	–
		IIa	-0.54	0.27	–	–	–	–
		IIb	-0.08	0.38	–	–	–	–
		III	-0.20	0.04	–	–	–	–
		IV	-0.20	0.03	–	–	–	–
Γ	$\frac{M_{\text{BH}}}{M_{\text{Sun}}}$	I	-0.05	0.58	–	–	–	–
		IIa	–	–	–	–	–	–
		IIb	–	–	–	–	–	–
		III	-0.05	0.58	–	–	–	–

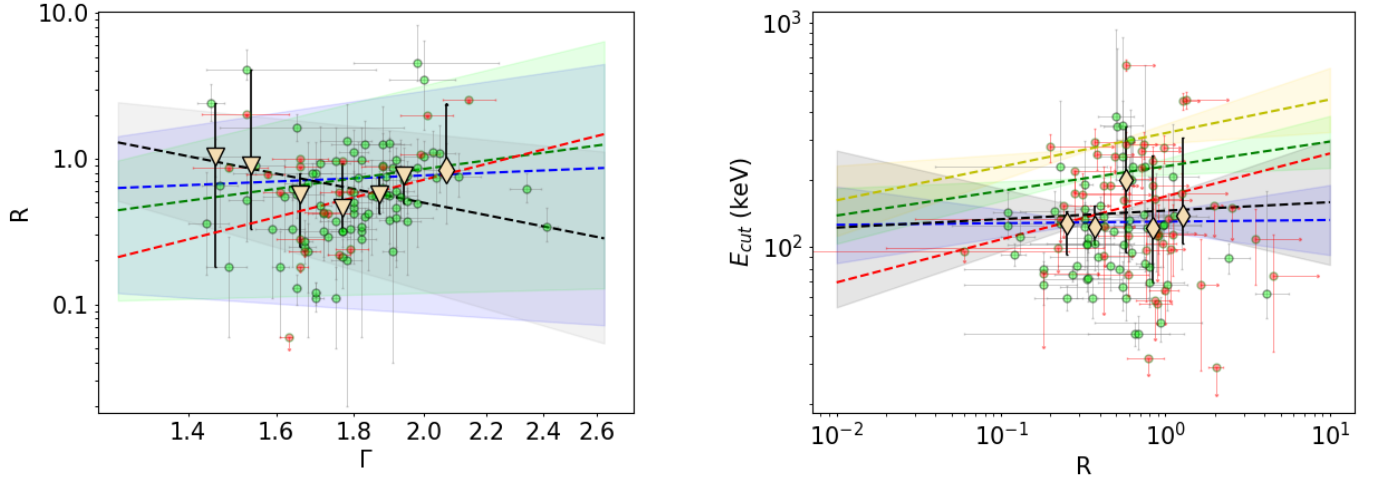


Figure 8. The relation between R - Γ (left panel) and E_{cut} - R (right panel). The lines and the shaded regions have similar descriptions as of 7.

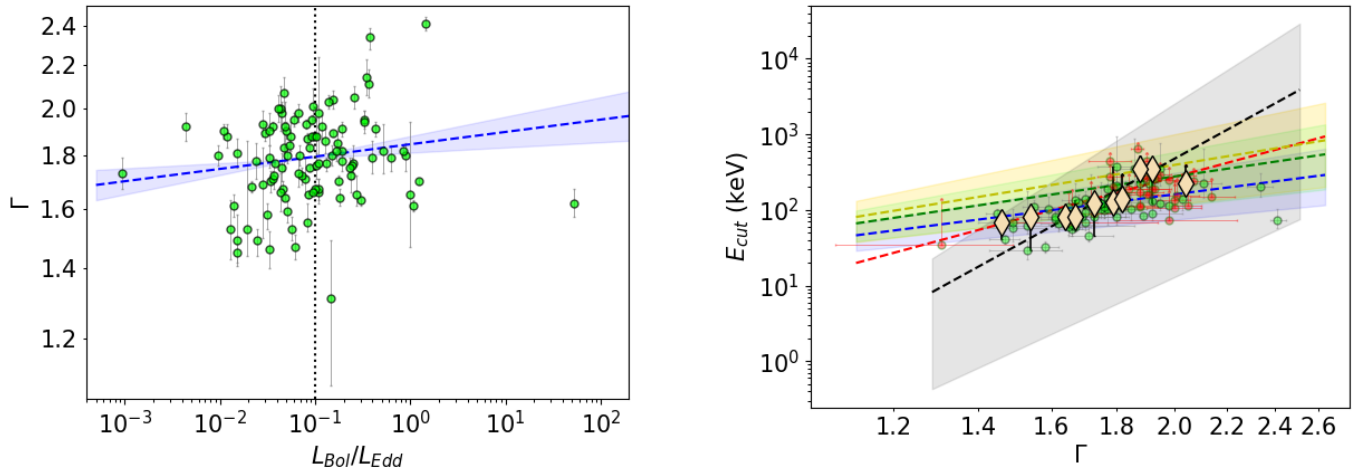


Figure 9. The relation between Γ - λ_{Edd} (left panel) and E_{cut} - Γ (right panel). The lines and the shaded regions have similar descriptions as of 7.

is valid only for low values of τ and kT_e . The authors also argued that if the origin of the X-ray emission is different than the thermal Comptonization, the typical relation between E_{cut} and kT_e may not hold. We show in the left panel of Fig. 5 the distribution of the ratio between E_{cut} to kT_e for 42 sources for which we could constrain both E_{cut} and kT_e . We found the ratio to vary between 2.33 and 5.35, with a median of 3.59 in 42 sources. In the right panel of Fig. 5 is shown the distribution of the sources in the E_{cut} versus kT_e plane. We excluded the sources with $E_{\text{cut}} > 300$ keV from this correlation analysis since at the high energy limit, the best fit kT_e values obtained using the Comptonization model produces comparative lower corona temperature than that obtained using a cut-off power law (Zdziarski et al. 2003; Fabian et al. 2015). To include the lower limits of E_{cut} and kT_e in our calculation we performed a survival analysis method using the non-parametric Kaplan-Maier Product Limit (KMPL) approach in *Python*⁵. The yellow points in the plot represent the median values of E_{cut} in different kT_e bins obtained from the survival analysis method using the KMPL approach. The errors in the median values of E_{cut} and kT_e were estimated in 95 per cent confidence. Also, shown in the same figure are the $E_{\text{cut}} = 2 kT_e$ (red dashed) and $E_{\text{cut}} = 3 kT_e$ (blue dashed) lines. From the linear least squares fit to the estimated median values of E_{cut} in different kT_e bins (black dashed line in Fig. 5), we found

$$E_{\text{cut}} = (3.80 \pm 0.53)kT_e + (8.15 \pm 16.51) \quad (1)$$

We calculated the Pearson’s correlation coefficient and the null hypothesis probability for no correlation to check the significance of the linear fit, and we found $r = 0.97$ and $p = 0.006$. We also used the *Astronomy SURVival Analysis (ASURV)* package (Feigelson & Nelson 1985) to take into account the lower limits in the E_{cut} and kT_e measurements. We derived the bivariate correlation and linear regression parameters using Spearman’s rho and the Schmitt method and found $E_{\text{cut}} = 3.54 kT_e + 13.99$. These observations thus indicate that for the sample of sources studied in this work, E_{cut} and kT_e maintain a strong correlation with most of our sources lying above the $E_{\text{cut}} = 3 kT_e$ line.

5. CORRELATION ANALYSIS

This section presents the correlation analysis between different best-fitted model parameters obtained using Model–1. We also discussed the correlation between

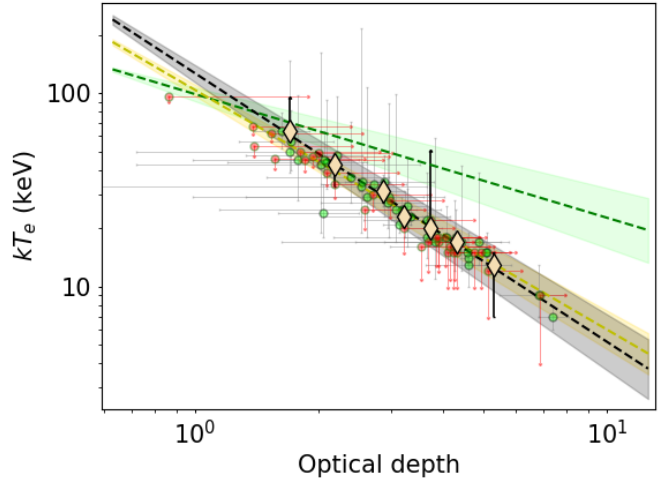


Figure 10. The relation between kT_e and τ . The green dots are the constrained values of the parameters, and the red dots denote the lower and upper limits of kT_e and τ , respectively. The yellow dashed line and the yellow shaded region are the linear fit to the constrained values of kT_e and τ , and the errors in the slope and the intercept of the linear fit (Method I). The beige diamond points represent the median values of kT_e in each bin of τ obtained from the survival analysis using the KMPL approach. The black dashed line and the black shaded region are the linear fit and the errors in the fit parameters to the median values of kT_e (Method II). The green dashed line and the green shaded region represent the linear fit and the errors in the slope and the intercept for the fit between two parameters considering both uncensored (including the corresponding asymmetric errors in kT_e) and censored (upper bound of $kT_e = 150$ keV) values of two parameters (Method III).

the coronal properties and the physical properties of the sources, such as λ_{Edd} and M_{BH} . For the latter, we had to exclude three sources from the correlation analysis, namely, ESO 416–G002, IRAS F12397+3333 and UGC 10120, as we did not find a black hole mass (M_{BH}) measurement for them from the literature. We adopted black hole mass estimates from the second data release of optical broad emission line measurements from the BASS survey (Mejía-Restrepo et al. 2022) except for ARK 564. The black hole mass for this source was taken from Denney et al. (2009).

For getting L_{bol} , we used the 2–10 keV intrinsic luminosity. The absorption and k –corrected intrinsic luminosities were converted to bolometric luminosities using the relation $\log(L_{\text{Bol}}) = 20 + \log(L_{2-10\text{keV}})$ (Vasudevan & Fabian 2007). The distribution of the logarithm of the Eddington ratio ($L_{\text{bol}}/L_{\text{Edd}} = \lambda_{\text{Edd}}$) for 109 sources is given in Fig. 6.

⁵ <https://medium.com/the-researchers-guide/survival-analysis-in-python-km-estimate-cox-ph-and-aft-model-5533843c5d5d>

The analysis of 112 sources using Model–1 revealed that E_{cut} could be constrained in 73 sources, while in the remaining 39 sources, only lower limits could be determined. These controlled E_{cut} measurements in 73 sources exhibited asymmetric errors, and E_{cut} in the remaining 39 sources only provided lower limits. From the measurements of kT_e also, we found constrained values in 42 sources, and the remaining 70 sources produced lower limits. In a few cases, we only found the upper limits of R . To account for the lower and upper limits in our correlation analysis, we used the KMPL approach, as described in Section 4. The median values of Parameter 2 (the dependent variable) were calculated using the KMPL method for each bin of Parameter 1 (the independent variable), in cases where only the dependent variable had upper or lower limits. When both the dependent and independent variables had upper and lower limits, the KMPL estimator calculated the survival function based on the data status of the independent variable (censored = 0, constrained = 1) and determined the median value for each bin. For the dependent variable, the probability function and median value were calculated for the corresponding bins of independent variables using the KMPL estimator. To tackle the unconstrained values of the independent and dependent variables in the correlation analysis, we used the survival statistics within the *ASURV FORTRAN* package as well to calculate Spearman’s rho correlation coefficient and the probability of no correlation. We derived the linear regression intercepts and slopes using the Schmitt method in *ASURV*.

Though the survival analysis is well-suited to take care of the limits in the correlation analysis, it does not consider the asymmetric errors in the analysis. Thus, it is essential to consider both the asymmetric errors and lower limits in the correlation analysis. Therefore, we employed a similar approach as described in Pal et al. (2022) to perform various correlation analyses and find the median of the parameters. The results of this analysis are given in Table 1.

We neglected the asymmetric errors associated with the controlled E_{cut} measurements in the initial approach and the lower limits. Instead, we solely considered the controlled best-fit values of E_{cut} and calculated the median values. We also performed correlation analysis using only those best-fit values between E_{cut} and other parameters by employing a logarithmic scale for fitting the parameters with a linear relation:

$$\log(y) = a\log(x) + b \quad (2)$$

In the second approach, we included both controlled and limited values in the correlation analysis by incorpo-

rating the survival analysis using the KMPL test and found the median values of the dependent parameters in each bin of the independent variable. We also used the *ASURV* package to handle both constrained and unconstrained values of the parameters in the correlation analysis. To assess the strength of the linear correlation in both cases (Method IIa and IIb in Table 1), we computed Spearman’s rank correlation coefficient (ρ) and the null hypothesis probability (p) for no correlation. We considered a correlation to be significant if p was less than 0.01.

In the third approach, we incorporated the asymmetric errors related to the controlled E_{cut} measurements and the lower limits of E_{cut} by simulating 10^5 random points within the range of $(E_{\text{cut}}^{\text{min}}, E_{\text{cut}}^{\text{max}})$ and $(E_{\text{cut}}^{\text{LL}}, E_{\text{cut}}^{\text{MAX}})$ respectively. For constrained E_{cut} with asymmetric errors, $E_{\text{cut}}^{\text{min}}$ and $E_{\text{cut}}^{\text{max}}$ represented the respective lower and upper bounds, while $E_{\text{cut}}^{\text{LL}}$ denoted the lower limit obtained from the model fit. The 10^5 random points were generated between the lower limit ($E_{\text{cut}}^{\text{LL}}$) and a hypothetical upper bound ($E_{\text{cut}}^{\text{MAX}}$) of 1000 keV. Following this approach, we calculated the median of E_{cut} for each run and then determined the mean of the median distribution. The statistical errors associated with the median values were calculated as the standard deviations of the 10^5 simulated median E_{cut} values.

In the fourth case, we handled the asymmetric errors corresponding to the constrained E_{cut} similarly as discussed in the third case. However, here, the upper bound $E_{\text{cut}}^{\text{MAX}}$ was set to 500 keV for cases where only lower limits were available. It was necessary to consider $E_{\text{cut}}^{\text{MAX}} = 1000$ keV in three sources for which the lower limit of E_{cut} exceeded 450 keV. The median and standard deviation of each run were calculated, and the mean of their distributions was determined. In both cases, the linear relation was fitted (using Equation 2) between E_{cut} and other parameters for each run, resulting in distributions of the slope (a), the intercept (b), the Spearman’s rank correlation coefficient (ρ), and the probability of no correlation (p). The median values from these distributions were used to represent the best-fit values of the correlation. All values and errors for the unweighted and simulated correlations are presented in Table 1.

We followed a similar approach for the other parameters also (Γ , R , and kT_e), simulating 10^5 points between the minimum and maximum bounds for the correlation analysis. In the case of the reflection fraction (R) and the coronal temperature (kT_e), respective upper and lower limits were obtained. During the correlation analysis, the lower bound of R was set at 0.01, and the upper bound of kT_e was set at 150 keV.

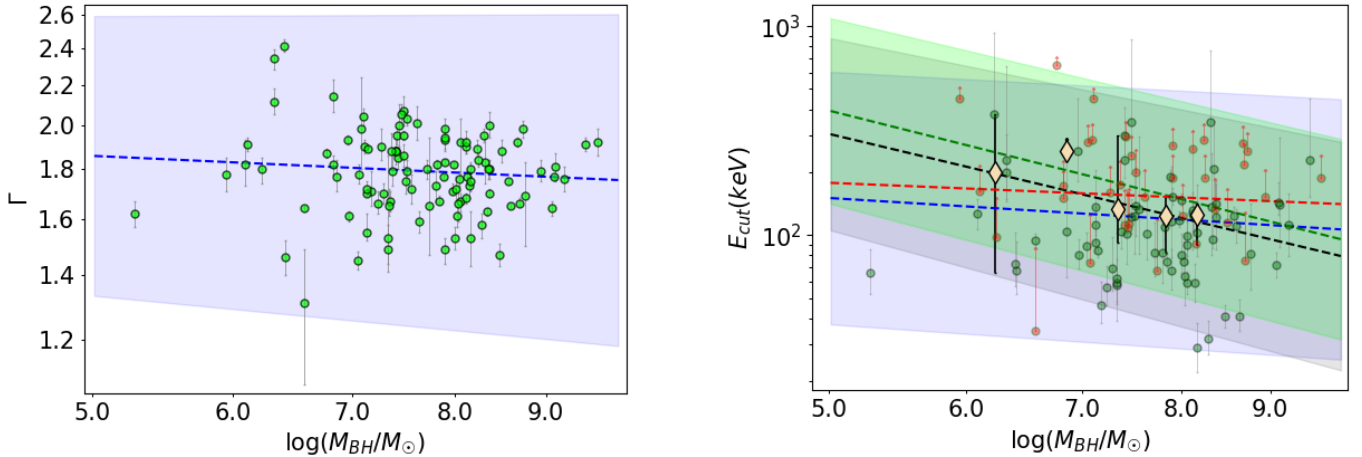


Figure 11. The relation between Γ and E_{cut} with the black hole mass. The lines and the shaded regions have similar descriptions as of 7.

Using the constrained values only, the median of E_{cut} as obtained from Model–1 was 104 ± 8 keV. The median of the unconstrained E_{cut} using the same model was 173 ± 18 keV. Considering the upper limit of 1000 keV for the censored values and the asymmetric errors associated with the controlled E_{cut} measurements, we obtained a median of 153 ± 8 keV for the full sample, 158 ± 11 keV for the moderately accreting system ($\lambda_{\text{Edd}} < 0.1$) and 150 ± 10 keV for the systems with higher accretion ($\lambda_{\text{Edd}} > 0.1$). Considering the upper limit of 500 keV, a median of 151 ± 7 keV was obtained for the entire sample. For the moderate ($\lambda_{\text{Edd}} < 0.1$) and high ($\lambda_{\text{Edd}} > 0.1$) accreting systems we obtained a median of 152 ± 10 keV and 147 ± 10 keV, respectively. Our result is consistent with the measurements of the median E_{cut} value obtained from the literature. For example, using a sample of unobscured Seyfert galaxies from *Swift*-BAT 70-month catalogue, Ricci et al. (2017) reported a median value of 210 ± 36 keV considering both censored and uncensored measurements. Using the XILLVER model to a total number of 195 Seyfert1 galaxies, Kamraj et al. (2022) found a median E_{cut} of 156 ± 13 keV.

We determined the median of kT_e as 24 ± 2 keV and 24 ± 3 keV respectively for the constrained and unconstrained best-fit values obtained using Model–2. Including the asymmetric errors and the lower limits by considering the upper bound of 150 keV, a median of 48 ± 5 keV was obtained. The distribution of E_{cut} and kT_e (constraints and the lower limits) are given in Fig. 2 and Fig. 4 respectively.

We also determined the median value of kT_e by analyzing a sample of 96 sources common to both this study and Ricci et al. (2018). We obtained the esti-

mate for E_{cut} from Ricci et al. (2018) and computed kT_e using Equation 1. The median value of kT_e for the subset with constrained values was 27 ± 7 keV, consistent with our findings of the median for only the controlled measurements. For the unconstrained best-fit value of kT_e as obtained from Ricci et al. (2018) the median was 29 ± 5 keV. For 67 sources where only lower limits were reported in Ricci et al. (2018), we considered both the asymmetric errors associated with the best-fit E_{cut} and an upper limit of 500 keV for cases where only a lower limit was reported, yielding a median kT_e of 85 ± 6 keV. This value is higher than what we observed for our sample but aligns with the results presented in Kamraj et al. (2022). The variance in median kT_e values between this study and Ricci et al. (2018) may be attributed to the higher proportion of unconstrained E_{cut} values in the latter work. Additionally, setting an upper limit of 500 keV for unconstrained cases biases the median value towards higher temperatures. The distribution of kT_e , as calculated using Equation 1 based on kT_e values from Ricci et al. (2018), is illustrated in Figure 6.

5.1. Correlation between E_{cut} and λ_{Edd}

We looked for a relation between E_{cut} and λ_{Edd} . Using all four methods of correlation analysis, we could not find any significant correlation between them. This is in agreement with the recent results in the literature (Tortosa, A. et al. 2018; Molina et al. 2019; Hinkle & Mushotzky 2021; Kamraj et al. 2022).

For AGN with moderate accretion ($\lambda_{\text{Edd}} < 0.1$) (Ricci et al. 2018), the observed spectral energy distribution can be explained by the standard optically thick geometrically thin accretion disk with $H/R \ll 1$, where H is the height of the disk at a radius R (Shakura &

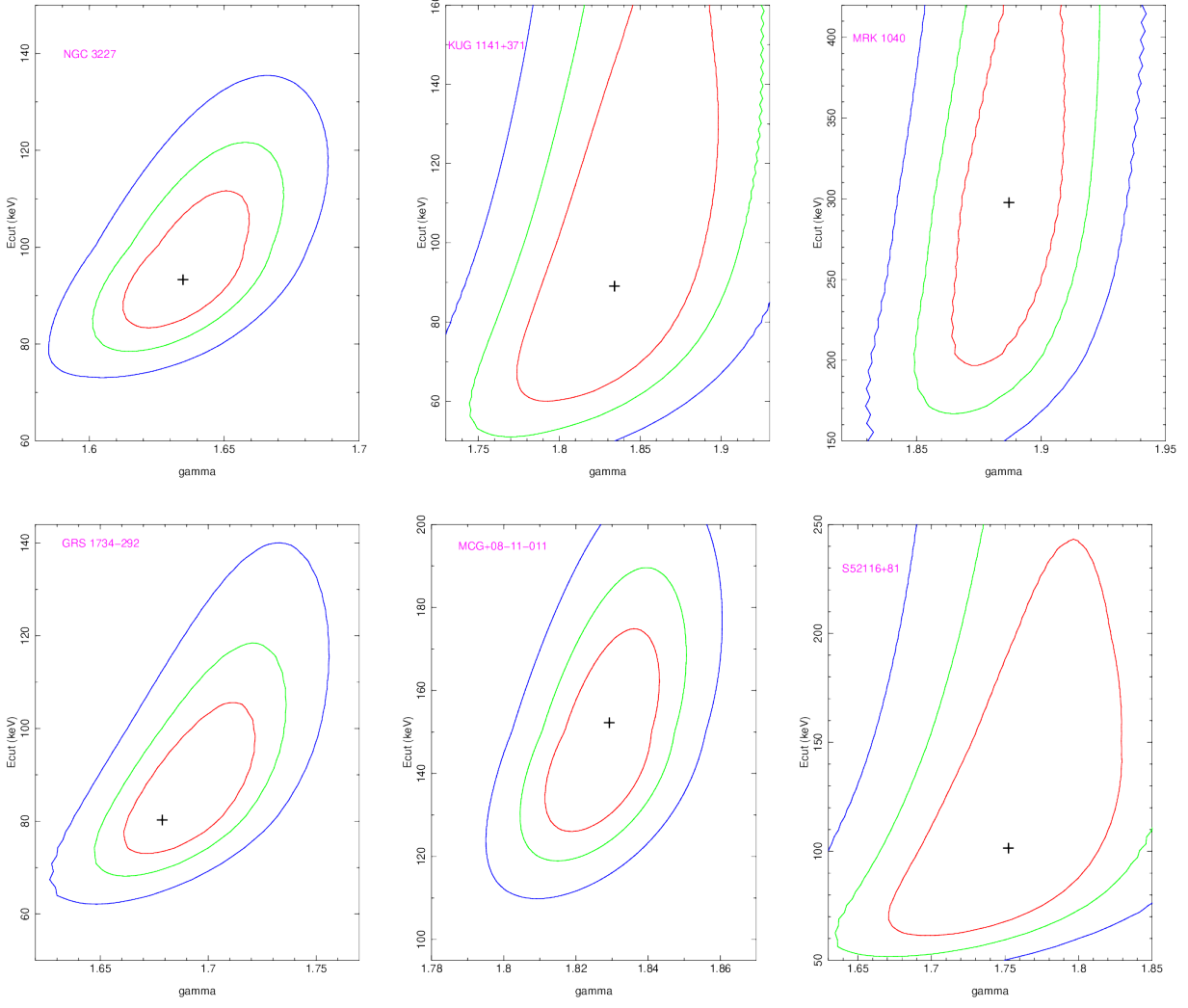


Figure 12. Confidence contours between E_{cut} and Γ obtained from Model–1 for six sources. The colour codes for the contours are as follows: red, green, and blue for 68% ($\Delta\chi^2 = 2.30$), 90% ($\Delta\chi^2 = 4.61$), and 99% ($\Delta\chi^2 = 11.8$) confidence levels, respectively. In each panel, the best-fit location is marked by the black plus.

Sunyaev 1973). But for AGN with higher λ_{Edd} , the accretion disk becomes geometrically thick with $H \leq R$ and therefore, the accretion flow nature is expected to differ from the moderately accreting ones (Paczynski & Bisnovaty-Kogan 1981; Muchotrzeb & Paczynski 1982; Abramowicz et al. 1988; Wang et al. 2014; Tortosa et al. 2022b). The emergent X-ray spectrum from AGN with thick and thin accretion disks is likely to be different, and hence, the connection between the accretion disk and corona in low and high accretion AGN could be different. To look for any differences in the corona between low and high accreting AGN, we divided our sample into moderately accreting AGN ($\lambda_{\text{Edd}} < 0.1$) and highly accreting AGN ($\lambda_{\text{Edd}} > 0.1$) and carried out linear fit to the data using Equation 2 in the E_{cut} versus λ_{Edd} plane. For the highly accreting sub-sample, we found no cor-

relation between E_{cut} and λ_{Edd} , which is expected for the sources with higher accretion rate (Wang & Netzer 2003). From the Spearman’s rank correlation test, we found ρ of 0.41 and a p of 0.009 considering only the controlled best-fit values E_{cut} in the moderately accreting systems ($\lambda_{\text{Edd}} < 0.1$), but including the asymmetric errors and the lower limits into consideration we did not find any significant relation between these two parameters (see Table 1 and fig. 7). Due to a limited number of median data points in both regions, we could not perform a survival analysis test. Using the *ASURV* package, we obtained ρ of 0.06 and a p of 0.55 for the entire sample; for the moderately accreting sub-sample, we obtained ρ of 0.11 and a p of 0.39 and for the highly accreting sub-sample a ρ of -0.16 and a p of 0.30 were calculated.

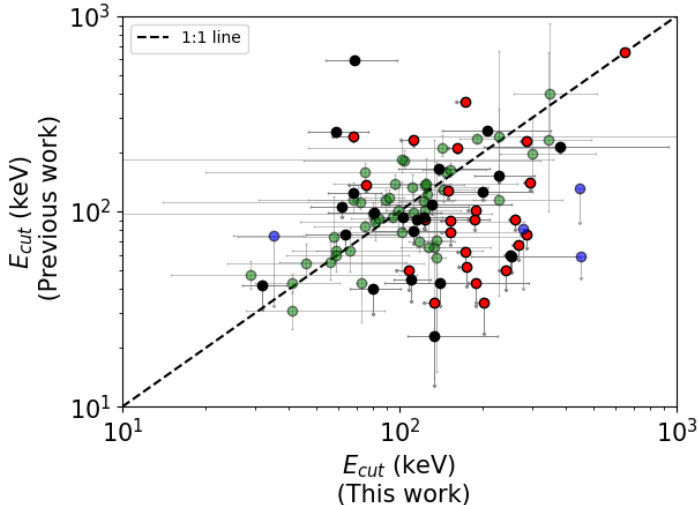


Figure 13. Plot of the estimated E_{cut} values from this work and those obtained from the literature. The green dots indicate the constrained E_{cut} values obtained from both this study and prior research. The red dots, signify the lower limits of E_{cut} values derived from both this study and the existing literature. The black dots denote the constrained E_{cut} values from this study and the lower limits of E_{cut} from the literature. The blue dots represent the constrained E_{cut} values from the literature and the lower limits of E_{cut} values from this study. The 1:1 line is also shown (the black dotted line) for reference.

5.2. Correlation between R and λ_{Edd}

We performed a simple linear fit to the data using Equation 2 to look for the correlation between R and λ_{Edd} . In a few cases, we could not constrain R ; rather, we found an upper limit. We considered both controlled values and the upper limits during the correlation analysis. Using only the controlled best-fit values, Spearman’s correlation analysis yielded a ρ of -0.28 and a p value of 0.01 . The survival analysis using the KMPL test indicated no correlation between R and λ_{Edd} with $\rho = -0.25$ and $p = 0.05$. Similar outcomes were also derived using the *ASURV* statistical analysis package. A Spearman’s correlation coefficient of -0.22 and $p = 0.02$ was obtained from the *ASURV* analysis. Using the third approach of the correlation analysis, we considered the asymmetric errors associated with the uncensored best-fit values of R and a lower bound of 0.01 in the cases where only the upper limit was found; we performed the linear fit for 10^5 times. From the distribution of ρ and p , we obtained the median of $\rho = -0.18$ and a $p = 0.07$. We thus conclude that using both uncensored and censored values of R , we could not get a meaningful correlation between R and λ_{Edd} . For the sources with moderate ($\lambda_{\text{Edd}} < 0.1$) and high ($\lambda_{\text{Edd}} > 0.1$) accretion rates, we

did not notice any significant correlation using methods I and III. Due to limited median data points, we could not perform the survival analysis for separate accreting regions. Using the *ASURV* package we obtained a $\rho = -0.25$ and a $p = 0.06$ for moderately accreting sub-sample and $\rho = -0.02$ and a $p = 0.88$ for highly accreting sub-samples. Thus, considering our sample of objects and dividing them into two different accreting systems, we conclude that the relation between R and λ_{Edd} is insignificant (see Fig. 7).

5.3. Correlation between R and Γ

We obtained an indication of a positive correlation between Γ and the reflection fraction in Table 1. We used Equation 2 to perform a linear fit between these two parameters. The fit gave us a ρ of 0.30 and a p of 0.002 , considering the controlled and upper limits of R . We obtained a positive correlation using only the constrained values with a ρ of 0.28 and a p of 0.009 . However, the KMPL and *ASURV* survival analysis denied the correlation with a ρ of -0.55 and 0.59 and a p of 0.26 and 0.03 , respectively. The correlation is plotted in the left panel of the Fig. 8

A study on the dependence of Γ on R has been done several times in past (Zdziarski et al. 1999; Beloborodov 1999; Malzac et al. 2001; Mattson et al. 2007; Dadina, M. 2008; Molina et al. 2009; Boissay, Rozenn et al. 2016; Lubiński et al. 2016; Moro et al. 2017; Zappacosta et al. 2018; Panagiotou, C. & Walter, R. 2019; Ezhikode et al. 2020; Kang et al. 2020). In most studies, the authors found a strong correlation between R and Γ . Although Mattson et al. (2007) argued that this strong positive correlation could be due to the model degeneracies rather than any physical act, Zdziarski et al. (1999) suggested that the observed correlation could be explained by considering an internal feedback mechanism, where the medium emitting seed photons for the primary X-ray emission also serves as the medium for reflection. Recently, from the analysis of 14 nearby bright Seyfert galaxies, Ezhikode et al. (2020) confirmed a strong correlation between R and Γ . The authors argued that the observed correlation could be either due to the Compton cooling process or the changing geometry of the disk-corona system. Recently, Kang et al. (2020) also reported a strong correlation between R and Γ . According to the authors, a stronger reflection and a softer X-ray spectrum could be predicted in the case of an outflowing corona.

5.4. Correlation between E_{cut} and R

We investigated the correlation between E_{cut} and R , performing the correlation analysis using the four methods mentioned above. Since the survival analysis with

the *ASURV* package does not handle cases where the dependent variable has lower limits and the independent variable has upper limits simultaneously, we performed the survival analysis under the following conditions: (1) only the dependent variable (E_{cut}) has a lower limit, (2) only the independent variable (R) has an upper limit, and (3) both dependent and independent have detected points. From the correlation analysis using the above-described methods i.e., considering only the constrained best-fit values of E_{cut} and R ; using the survival analysis test (KMPL and *ASURV* package); considering the asymmetric errors and the constant upper and lower limits of $E_{\text{cut}}^{\text{MAX}}$ to be 1000 keV and $R^{\text{MIN}} = 0.01$ and $E_{\text{cut}}^{\text{MAX}} = 500$ keV and $R^{\text{MIN}} = 0.01$, we obtained $p = 0.84, 0.66, 0.08, 0.12$ and 0.12 respectively, suggesting no significant correlation between these two parameters (see Fig. 8). Previously, [Hinkle & Mushotzky \(2021\)](#) reported a mild anti-correlation between E_{cut} and R .

5.5. Correlation between Γ and λ_{Edd}

Next we examined the correlation between Γ and λ_{Edd} . Considering the whole sample, we noticed a positive trend, though insignificant, between these two parameters. The correlation analysis produced a ρ of 0.17 and a p value of 0.08. We also conducted an analysis accounting for the errors in the measurements of Γ . Still, it did not yield any significant correlation, which agrees with what was reported by [Tortosa, A. et al. \(2018\)](#). No significant correlation was found in the moderate ($\lambda_{\text{Edd}} < 0.1$) and high ($\lambda_{\text{Edd}} > 0.1$) Eddington ratio subsets. It is worth noting that previous studies ([Shemmer et al. 2006, 2008](#); [Risaliti et al. 2009](#); [Trakhtenbrot et al. 2017](#); [Ricci et al. 2018](#)) have reported a positive correlation between these two parameters. The correlation is plotted in Fig 9.

5.6. Correlation between E_{cut} and Γ

The correlation between E_{cut} and Γ is shown in Fig. 9. From correlation analysis of the linear fit, we obtained a ρ of 0.69 and a p value of 1.75×10^{-11} considering only the controlled measurements of E_{cut} and Γ , suggesting a significant correlation between these two parameters. The KMPL test of the survival analysis also indicated a strong correlation between E_{cut} and Γ with $\rho = 0.99$ and $p = 1.46 \times 10^{-5}$. The statistical analysis using the package *ASURV* derived a $\rho = 0.57$ with $p = 0.0$, suggesting a strong correlation between these two parameters. Using the third approach, we found a ρ of 0.60 and a p value of 4.11×10^{-12} . We also obtained a significant correlation between them using our fourth approach and got a ρ of 0.61 and a p value of 1.75×10^{-12} . In the third and fourth cases, the errors in Γ are taken care of by

producing 10^5 random points between Γ^{min} and Γ^{max} at each run, where Γ^{min} and Γ^{max} are the respective lower and upper bounds of Γ .

Similar studies on the correlation analysis between the temperature of the corona and Γ are available in the literature. From a study of 19 Seyfert galaxies using data from *NuSTAR*, [Tortosa, A. et al. \(2018\)](#) found no significant correlation between kT_e and Γ . In contrast, [Molina et al. \(2019\)](#) found a positive correlation between E_{cut} and Γ based on spectral analysis of 18 Seyfert galaxies using data from *Swift-XRT* and *NuSTAR*. The authors suggested that the correlation observed in their sample could result from the systematic uncertainties affecting one of the two parameters or the lack of high-quality data in the soft X-ray regime. A few recent studies reported positive correlation between E_{cut} and Γ ([Kamraj et al. 2018](#); [Hinkle & Mushotzky 2021](#); [Kang & Wang 2022](#)). Of these, [Kamraj et al. \(2018\)](#) analysed a total of 46 Seyfert 1 galaxies, while [Hinkle & Mushotzky \(2021\)](#) and [Kang & Wang \(2022\)](#) carried out spectral analysis of 33 and 60 sources, respectively. While [Kang & Wang \(2022\)](#) found a relatively strong correlation between E_{cut} and Γ , it is rather weak, as reported in [Kamraj et al. \(2018\)](#) and [Hinkle & Mushotzky \(2021\)](#). This may be due to the small sample size and domination of the lower limits in the E_{cut} measurements in their studies. While our study produced a stronger correlation between these two parameters for a large number of sources in which we could tightly constrain Γ in all of them and E_{cut} in most of them, the influence of degeneracy between these two parameters could not be neglected. To check the degeneracy between E_{cut} and Γ in our sample, we generated contours between these two parameters for all the sources, six of which are presented in Figure 12. The contours are elliptical and have smooth levels, suggesting the parameters were well-constrained. While we noticed weak degeneracy in the contour plots, we managed to constrain both parameters effectively in the majority of cases. This implies that any potential artefacts between them may be minor, given the substantial number of sources analyzed in this study.

From an analysis of multiple epochs of observations on a source SWIFT J2127.4+5654, [Kang et al. \(2021\)](#) found a Λ shaped pattern. According to the authors, up to $\Gamma < 2.05$, the source showed a “steeper-when-hotter” behaviour, while beyond $\Gamma > 2.05$, the source showed a “softer-when-cooler” behaviour. Though the finding of [Kang et al. \(2021\)](#) is from multiple observations of a single source, we attempted to check the prevalence of such a trend in our sample of sources. There are only a few sources in our sample with $\Gamma > 2.05$, and the statistical test resulted in a negative trend between

E_{cut} and Γ . However, we could not conclude about the significance of the anti-correlation noticed since very few sources were found in the $\Gamma > 2.05$ region. A systematic and homogeneous analysis of many sources is needed to confirm this finding.

5.7. Correlation between kT_e and τ

We calculated τ using the following Equation (Zdziarski et al. 1996; Życki et al. 1999)

$$\tau = \sqrt{\frac{9}{4} + \frac{3}{\theta \left[\left(\Gamma + \frac{1}{2} \right)^2 - \frac{9}{4} \right]}} - \frac{3}{2} \quad (3)$$

where $\theta = kT_e/m_e c^2$. Considering only the constrain values of kT_e we found a strong negative correlation between kT_e and τ (see Fig. 10). Spearman's rank correlation analysis yielded a ρ of -0.96 with a p value of 1.82×10^{-23} . Earlier, Tortosa, A. et al. (2018) also found a strong anti-correlation between these parameters for slab and spherical geometries. The authors fitted a similar linear relation in the kT_e vs τ plane and reported,

$$a = -0.7 \pm 0.2; b = 1.8 \pm 0.1. \quad (4)$$

for the spherical geometry. We also found similar values of a and b from our linear fit to the data points,

$$a = -1.24 \pm 0.07; b = 2.02 \pm 0.03. \quad (5)$$

From the survival analysis, we obtained a ρ of -0.99 and $p = 1.40 \times 10^{-24}$ indicating a strong anti-correlation between these two parameters. We could not perform the statistical test using the *ASURV* package since it does not calculate the correlation when the dependent variable (kT_e) has a lower limit, and the independent variable (τ) has an upper limit simultaneously. Using an upper limit of 150 keV for unconstrained kT_e , we confirmed a strong negative correlation between kT_e and τ with a ρ of -0.66 and $p = 1.89 \times 10^{-10}$ (see Table 1).

6. COMPARISON WITH PREVIOUS WORK

This section compares the best-fit values of E_{cut} from this work with those available in the literature. Of the 112 sources analysed in this work, we could constrain E_{cut} for 73 sources. For all these 112 sources, E_{cut} measurements were carried out using the most recent physical models (*xillver/relxill/(relxill+xillver)*) available. In the past, most of these nearby unobscured AGN were analysed vividly using mostly phenomenological models such as *pearrav/pexmon* etc. Here, we present a comparison of the E_{cut} measurements obtained from our analysis with those available in the literature in Table 3.

For the majority of the sources in literature, E_{cut} was reported using the broad-band spectral analysis of the

NuSTAR data in conjunction with the soft X-ray data from several other instruments, such as *XMM-Newton*, *Swift-XRT* etc. (Fabian et al. 2015; Turner et al. 2018; Molina et al. 2019; Porquet, D. et al. 2021; Hinkle & Mushotzky 2021; Kamraj et al. 2022; Diaz, Y. et al. 2023). In a few references E_{cut} was obtained from the analysis of the *Swift-BAT*, *BeppoSAX* and *INTEGRAL* broad-band X-ray data (Dadina, M. 2007; Ricci et al. 2017; Molina et al. 2013; Malizia et al. 2014). As seen from Table 3, our results from the analysis of only the *NuSTAR* data agrees with the previous analysis (see Fig. 13). Our derived E_{cut} also matches with those already reported in the literature using only the *NuSTAR* data (Tortosa, A. et al. 2018; Kamraj et al. 2018; Baloković et al. 2020; Ezhikode et al. 2020; Kang et al. 2020; Akylas, A. & Georgantopoulos, I. 2021). Since these sources are known to be variable, we noticed a mismatch in the E_{cut} values in a few cases where the epoch of observations differs from those used in this work. In Fig. 13, we plotted the constrained E_{cut} values obtained both from this work and the previous work with green dots; the red dots represent the lower limit of E_{cut} from both this work and the literature, The black ones represent the constrained E_{cut} from this work and the lower limit of E_{cut} from the literature. Finally, we plotted the constrained E_{cut} from literature and the lower limit of E_{cut} values from this work using blue dots. The grey lines indicated the errors and the lower limits. Most of the sources lie around the 1:1 line (black dotted line), except for a few red dots, representing the lower limit obtained from this work is lower than that found in the literature.

7. DISCUSSION

We examined the correlations between various coronal properties, as well as between coronal parameters and the physical properties of the sources studied in this work. We also examined whether moderately accreting sources ($\lambda_{\text{Edd}} < 0.1$) have different X-ray emission characteristics relative to the highly accreting sources ($\lambda_{\text{Edd}} > 0.1$).

From Table 1, we noticed a significant correlation between E_{cut} and Γ (see Fig. 9) for the entire sample of sources. Such positive correlation between E_{cut} and Γ was also reported in the past (Perola et al. 2002; Kamraj et al. 2018; Middei et al. 2019; Hinkle & Mushotzky 2021; Kang & Wang 2022). However, there are instances where the observed correlation between E_{cut} and Γ was not definitively established (Molina et al. 2009; Ricci et al. 2017; Tortosa, A. et al. 2018; Kamraj et al. 2022). According to Middei et al. (2019), the observed correlation might result from potential systematic uncertainties associated with one of the two parameters. The

observed correlation could also be accounted for by the presence of an optically thin corona. Furthermore, the relationship between these two variables remains incomprehensible even for individual AGN (Kang et al. 2021).

From our analysis, another strong anti-correlation was found between kT_e and τ (see Fig. 10). Such negative correlation between kT_e and τ is already known in literature and is attributed to either the fact that the cooling rate is more efficient in corona with higher opacity or to the variation in the intrinsic disk emission from the sources (Tortosa, A. et al. 2018; Kang & Wang 2022). The positive correlation between E_{cut} and Γ suggests that a steeper spectrum typically corresponds to a hotter corona. The corona must become optically thinner for a spectrum to steepen, indicating a hotter environment. Consequently, the inverse correlation between kT_e and τ indicates that a sustainable hotter corona has lower opacity and a softer spectrum. These findings challenge the traditional notion that a corona in a higher accreting system tends to be cooler due to its rapid interaction with the seed disk photons, resulting in a softer X-ray spectrum. Therefore, the observed correlation is likely driven by variations in the intrinsic disk emission across different sources.

We therefore examined the correlations between E_{cut} and Γ with the physical parameters of the sources (λ_{Edd} and M_{BH}) (see Table 1 and Fig. 11). In the past, several authors have reported a positive correlation between Γ and λ_{Edd} (Brandt et al. 1997; Shemmer et al. 2006, 2008; Risaliti et al. 2009; Brightman et al. 2013; Brightman et al. 2016; Trakhtenbrot et al. 2017). Most authors have utilized a similar linear relationship, as described in Equation 2, to investigate the connection between these two parameters. We found a slope (b) of 0.26, with an ρ -value of 0.17 and a p-value of 0.08 from Spearman’s correlation analysis. Our findings align with the slope reported by Shemmer et al. (2008) and Brightman et al. (2013), both of whom identified a similar slope of approximately 0.3 from the correlation analyses between Γ and λ_{Edd} . However, Risaliti et al. (2009), in their examination of *SDSS* quasars with archival *XMM-Newton* observations, reported a steeper slope ($b \sim 0.6$). More recently, Trakhtenbrot et al. (2017) employed *BASS* data and found a considerably weaker and flatter correlation ($b \sim 0.15$). Trakhtenbrot et al. (2017) argued that as M_{BH} decreases, the number of optical-UV seed photons increases and due to the production of a larger amount of seed photons, the corona interacts with it rapidly, and that in turns cools the corona down resulting a softer spectrum. Therefore, based on this argument, one should expect a positive correlation between Γ and M_{BH} . From the analysis of our sample of sources, we

could not confirm such a trend. We also explored the relationship between E_{cut} and λ_{Edd} . When analyzing the entire sample, as well as the higher and lower accretion regimes separately, no significant correlation was observed between these two parameters. These findings are consistent with similar results reported in the literature (Tortosa, A. et al. 2018; Middei et al. 2019; Hinkle & Mushotzky 2021; Kamraj et al. 2022). Additionally, we did not find any significant correlation between E_{cut} and M_{BH} . Therefore, the lack of significant correlations between the coronal parameters and the physical properties of the sources suggests that the observed significant correlation between E_{cut} and Γ , with τ decreasing significantly as kT_e increases, may not be due to intrinsic changes in the sources themselves or due to the Compton cooling effect (i.e., cooler corona has steeper spectrum), but rather due to morphological variations in the corona across different sources. A larger dataset is needed to better understand the nature of these observed correlations.

8. SUMMARY

In this study, we analysed the 3–79 *NuSTAR* spectra of a sample of 112 Seyfert 1 galaxies, the data for which were publicly available between August 2013 and May 2022 in *NuSTAR* Master Catalog. The motivation is to carry out a systematic study of the coronal properties of Seyfert 1 type AGN. From the physical model fits to the spectrum of 112 sources, we could constrain E_{cut} in 73 sources. We used physically motivated Comptonization models to derive various physical coronal properties. We could constrain kT_e in 42 sources. The results of this study are summarized below:

1. Using Model–1, we estimated the median value of Γ to be 1.79 ± 0.02 . Using Model–2, we derived a median of 1.86 ± 0.01 for Γ .
2. The median values, as calculated using Model-1, were 104 ± 8 keV and 173 ± 18 keV for the best-fitted constrained and unconstrained values of E_{cut} , respectively. When considering an upper limit of 1000 keV for the censored E_{cut} measurements and accounting for the asymmetric errors in the constrained E_{cut} values, the median value for E_{cut} across the entire sample was determined to be 153 ± 8 keV. In the sub-sample with moderate accretion rates ($\lambda_{\text{Edd}} < 0.1$), the median E_{cut} was found to be 158 ± 11 keV, while in the sub-sample with high accretion rates ($\lambda_{\text{Edd}} > 0.1$), the median E_{cut} is 150 ± 10 keV.
3. The median values of constrained and unconstrained kT_e as estimated using Model–2 were

24 ± 2 keV and 24 ± 3 keV respectively. Using both the controlled and censored kT_e (considering an upper bound of 150 keV), the median value of kT_e was calculated to be 48 ± 5 keV.

4. For our sample of sources we found E_{cut} is strongly correlated with kT_e as $E_{\text{cut}} = (3.80 \pm 0.53) kT_e + (8.15 \pm 16.51)$. This is in agreement with the notion that the X-ray spectra of AGN are related to the temperature of the corona as $E_{\text{cut}} = 2-3 kT_e$. However, a large number of sources analysed in this work lie above the $E_{\text{cut}} = 3 kT_e$ line, which is deviant from the general notion of $E_{\text{cut}} = 2-3 kT_e$. Analysis of more sources is needed to confirm this.
5. For our entire sample, we found a strong correlation between E_{cut} and Γ .
6. We found a significant anti-correlation between kT_e and τ . The best-fit relation yielded a slope and intercept of -1.24 ± 0.07 and 2.02 ± 0.03 .
7. All these correlations indicate that an optically thin corona is necessary to sustain a hotter corona with a steeper spectrum. With the increasing accretion rate, the hotter corona could move vertically away from the central engine and become

optically thinner. A systematic and homogeneous analysis of a larger sample of sources is needed to establish the correlation observed between various physical quantities, thereby enhancing our understanding of AGN corona.

We thank the anonymous referee for their very helpful comments on the manuscript. We thank the *NuSTAR* Operations, Software and Calibration teams for support with the execution and analysis of these observations. This research has made use of the *NuSTAR* Data Analysis Software (NuSTARDAS) jointly developed by the ASI Science Data Center (ASDC, Italy) and the California Institute of Technology (USA). C.R. acknowledges support from the Fondecyt Regular (grant 1230345) and ANID BASAL (project FB210003). This research has used data and/or software provided by the High Energy Astrophysics Science Archive Research Center (HEASARC), a service of the Astrophysics Science Division at NASA/GSFC.

Facilities: *NuSTAR*
Software: FTOOLS ⁶

APPENDIX

A. ADDITIONAL TABLE

⁶ <https://heasarc.gsfc.nasa.gov/ftools/>

Table 2. Details of the sources analysed in this work. The columns are (1) the name of the source, (2) right ascension (h:m:s), (3) declination (d:m:s), (4) redshift, (5) type of the source, (6) observation ID (OBSID), (7) count rate (counts/sec) (8) exposure time in sec (9) black hole mass, and (10) the Eddington ratio. Some of the information, including the right ascension, declination, and z , are from SIMBAD⁸.

Source	α_{2000}	δ_{2000}	z	Type	OBSID	Count rate	Exposure	M_{BH}/M_{\odot}	$L_{\text{bol}}/L_{\text{edd}}$
1H 0419-577	04 26 00.71	-57 12 01.76	0.104	Sy1.0	60101039002	0.4	169462	8.06	0.05
1H1934-063	19 37 33.02	-06 13 04.80	0.01	Sy1.0	60702018006	0.52	65521	6.33	0.37
2E1739.1-1210	17 41 55.25	-12 11 56.58	0.037	Sy1.2	60160670002	0.3	21366	8.23	0.03
2MASS J1830231+731310	18 30 23.16	+73 13 10.71	0.123	Sy1.0	60464150002	0.16	26019	—	—
2MASSJ17485512-3254521	17 48 55.13	-32 54 52.10	0.02	Sy1.0	60160677002	0.27	21801	8.02	0.01
2MASXJ04372814-4711298	04 37 28.16	-47 11 29.48	0.053	Sy1.0	30001061002	0.12	73821	7.89	0.04
2MASXJ11324928+1017473	11 32 49.27	+10 17 47.27	0.044	Sy1.0	60061212002	0.05	20469	7.44	0.04
2MASXJ12313717-4758019	12 31 37.14	-47 58 02.00	0.028	Sy1.0	60160498002	0.14	19356	7.41	0.06
2MASXJ15295830-1300397	15 29 58.33	-13 00 39.78	0.104	Sy1.0	60160617002	0.15	24227	7.52	0.63
2MASXJ1802473-145454	18 02 47.30	-14 54 55.00	0.035	Sy1.0	60160680002	0.59	19958	7.56	0.24
2MASXJ18470283-7831494	18 47 02.69	-78 31 49.60	0.074	Sy1.0	60160699002	0.22	21505	8.37	0.07
2MASXJ18560128+1538059	18 56 01.28	+15 38 05.90	0.084	Sy1.0	60160701002	0.22	21352	8.47	0.06
2MASXJ19380437-5109497	19 38 04.39	-51 09 49.38	0.04	Sy1.0	60160716002	0.24	21830	7.43	0.17
2MASXJ21192912+3332566	21 19 29.12	+33 32 56.67	0.051	Sy1.5	60061358002	0.23	21483	7.71	0.15
2MASXJ21355399+4728217	21 35 54.02	+47 28 21.89	0.025	Sy1.0	60160761002	0.24	18704	7.24	0.11
2MASXJ23013626-5913210	23 01 36.23	-59 13 21.08	0.15	Sy1.8	60160814002	0.16	19500	—	—
3C 109	04 13 40.34	+11 12 14.78	0.306	Sy1.8	60301011004	0.17	89150	9.07	0.18
3C 111	04 18 21.27	+38 01 35.80	0.05	Sy1.0	60202061004	0.74	49361	8.57	0.09
3C 120	04 33 11.09	+05 21 15.61	0.034	Sy1.0	60001042003	1.31	127716	7.99	0.19
3C 206	08 39 50.58	-12 14 34.32	0.198	Sy1.2	60160332002	0.29	17390	9.22	0.10
3C 227	09 47 45.14	+07 25 20.59	0.086	Sy1.5	60061329002	0.3	17195	8.94	0.03
3C 380	18 29 31.78	+48 44 46.16	0.692	Sy1.0	60160690002	0.13	19610	—	—
3C 382	18 35 03.38	+32 41 46.85	0.058	Sy1.0	60001084002	0.82	82583	8.6	0.08
3C 390.3	18 42 08.99	+79 46 17.12	0.06	Sy1.0	60001082003	1.03	47557	9.1	0.04
6dFJ1254564-265702	12 54 56.37	-26 57 02.10	0.059	Sy1.0	60363001002	0.14	20296	8.28	0.03
ARK 120	05 16 11.40	-00 08 59.15	0.03	Sy1.0	60001044004	0.99	65453	8.31	0.06

Table 2 *continued*

Table 2 (continued)

Source	α_{2000}	δ_{2000}	z	Type	OBSID	Count rate	Exposure	M_{BH}/M_{\odot}	$L_{\text{bol}}/L_{\text{edd}}$
Ark 241	10 21 40.25	-03 27 13.75	0.041	Sy1.0	60160392002	0.18	20329	8.5	0.01
ARK 564	22 42 39.35	+29 43 31.31	0.025	Sy1.8	60401031004	0.28	408958	6.41	1.44
CGCG229-015	19 05 25.94	+42 27 39.76	0.028	Sy1.0	60160705002	0.13	21992	7.18	0.08
ESO 025-G002	18 54 40.26	-78 53 54.10	0.029	Sy1.0	60160700002	0.24	27978	7.35	0.11
ESO 031-G008	03 07 35.34	-72 50 02.50	0.028	Sy1.0	60160141002	0.19	31655	7.1	0.15
ESO 209-G012	08 01 57.97	-49 46 42.39	0.04	Sy1.5	60160315002	0.29	23715	8.11	0.05
ESO 323-G077	13 06 26.12	-40 24 52.59	0.015	Sy1.5	60202021006	0.13	43403	7.05	0.02
ESO 416-G002	02 35 13.45	-29 36 17.25	0.059	Sy1.9	60061340002	0.1	20606	—	—
ESO 511-G030	14 19 22.40	-26 38 41.13	0.022	Sy1.0	60502035008	0.12	41807	7.29	0.03
ESO381-G007	12 40 46.96	-33 34 11.84	0.055	Sy1.5	60160508002	0.12	21250	8.03	0.04
FAIRALL 1146	08 38 30.77	-35 59 33.33	0.032	Sy1.5	60061082002	0.34	21278	7.52	0.14
Fairall 51	18 44 53.98	-62 21 52.87	0.014	Sy1.0	60402014002	0.24	63532	7.33	0.02
GRS 1734-292	17 37 28.38	-29 08 02.11	0.021	Sy1.0	60301010002	0.15	26020	7.84	0.10
H1821+643	18 21 57.21	+64 20 36.22	0.297	Sy1.0	60160683002	0.37	22173	9.48	0.19
HE 1143-1810	11 45 40.46	-18 27 14.96	0.033	Sy1.0	60302002006	0.69	23096	7.38	0.40
HE1136-2304	11 38 51.00	-23 21 35.34	0.027	Sy	80002031003	0.26	63565	6.97	1.09
IC 1198	16 08 36.38	+12 19 51.60	0.033	Sy1.5	60361014002	0.11	26973	7.51	0.04
IC 4329A	13 49 19.26	-30 18 34.21	0.016	Sy1.2	60001045002	2.61	162390	7.88	0.11
IGR J14471-6414	14 46 28.20	-64 16 24.00	0.053	Sy1.2	60061257002	0.1	15042	7.61	0.09
IGRJ4552-5133	14 55 17.51	-51 34 15.18	0.016	Sy1.0	60401022002	0.23	100942	6.96	0.08
IGRJ19378-0617	19 37 33.02	-06 13 04.80	0.01	Sy1.0	60101003002	0.52	65521	6.33	0.37
IRAS 05589+2828	06 02 10.47	+28 28 19.40	0.033	Sy1.0	60061062002	0.78	29276	8.32	0.05
IRAS 09149-6206	09 16 09.36	-62 19 29.56	0.057	Sy1.0	90401630002	0.4	112121	8.76	0.03
IRAS F12397+3333	12 42 10.60	+33 17 02.66	0.044	Sy1.0	60501007002	0.16	48709	—	—
IRAS04124-0803	04 14 52.66	-07 55 39.68	0.039	Sy1.0	60761001002	0.32	18345	8	0.06
IRAS04392-2713	04 41 22.53	-27 08 19.33	0.084	Sy1.0	60160201002	0.19	19553	9.63	0.00
KUG 1141+371	11 44 29.87	+36 53 08.61	0.038	Sy1.0	90601618002	0.28	38562	8.06	0.05
MCG-06-30-15	13 35 53.76	-34 17 44.16	0.008	Sy1.2	60001047005	0.8	23267	6.09	0.52
MCG+05-40-026	17 01 07.77	+29 24 24.58	0.036	Sy1.0	60061276002	0.12	21000	6.86	0.25
MCG+08-11-011	05 54 53.61	+46 26 21.61	0.02	Sy1.5	60201027002	1.23	97921	7.9	0.09

Table 2 continued

Table 2 (continued)

Source	α_{2000}	δ_{2000}	z	Type	OBSID	Count rate	Exposure	M_{BH}/M_{\odot}	$L_{\text{bol}}/L_{\text{edd}}$
MR 2251–178	22 54 05.88	–17 34 55.40	0.064	Sy1.0	60102025002	1.22	23112	8.34	0.30
MRK 1040	02 28 14.46	+31 18 41.46	0.017	Sy1.5	60101002004	0.69	64242	7.41	0.10
MRK 1044	02 30 05.52	–08 59 53.20	0.016	Sy1.0	60401005002	0.22	267078	6.23	0.90
MRK 110	09 25 12.84	+52 17 10.38	0.036	Sy1.0	60201025002	0.98	184563	7.13	1.24
MRK 1148	00 51 54.76	+17 25 58.50	0.064	Sy1.0	60160028002	0.5	22087	8.05	0.25
MRK 1310	12 01 14.35	–03 40 41.01	0.02	Sy1.0	60160465002	0.23	21131	6.83	0.17
MRK 1383	14 29 06.57	+01 17 06.15	0.086	Sy1.0	60501049002	0.18	95955	8.67	0.04
MRK 1392	15 05 56.55	+03 42 26.33	0.036	Sy1.0	60160605002	0.14	21084	7.9	0.03
MRK 1393	15 08 53.95	–00 11 49.00	0.054	Sy1.5	60376005002	0.21	30816	7.42	0.32
MRK 205	12 21 44.07	+75 18 38.24	0.071	Sy1.0	60160490002	0.21	20372	8.11	0.12
Mrk 279	13 53 03.43	+69 18 29.41	0.031	Sy1.5	60601011004	0.16	200632	7.89	0.02
MRK 290	15 35 52.40	+57 54 09.51	0.03	Sy1.0	60061266004	0.2	26348	7.64	0.05
MRK 335	00 06 19.53	+20 12 10.61	0.025	Sy1.2	60001041005	0.17	93022	7.08	0.11
MRK 359	01 27 32.52	+19 10 43.83	0.017	Sy1.5	60402021002	0.15	52526	6.11	0.43
Mrk 509	20 44 09.75	–10 43 24.72	0.034	Sy1.5	60101043002	1.19	165885	8.13	0.13
MRK 590	02 14 33.56	–00 46 00.18	0.026	Sy1.2	80502630002	0.33	68123	8.12	0.02
MRK 595	02 41 34.87	+07 11 13.85	0.027	Sy1.5	60160119002	0.06	21298	6.58	0.15
MRK 684	14 31 04.78	+28 17 14.12	0.045	Sy1.0	60160586002	0.08	20497	6.83	0.34
MRK 704	09 18 25.99	+16 18 19.63	0.029	Sy1.5	60061090002	0.27	21524	8.35	0.01
MRK 732	11 13 49.75	+09 35 10.58	0.029	Sy1.5	60061208002	0.21	26359	7.06	0.19
MRK 79	07 42 32.82	+49 48 34.78	0.022	Sy1.2	60601010002	0.58	65805	7.48	0.13
MRK 813	14 27 25.05	+19 49 52.26	0.11	Sy1.0	60160583002	0.21	24562	8.73	0.07
MRK 817	14 36 22.08	+58 47 39.39	0.031	Sy1.5	60601007002	0.21	135300	7.74	0.99
MRK 841	15 04 01.19	+10 26 15.78	0.036	Sy1.5	60101023002	0.44	23419	8.16	0.05
MRK 876	16 13 57.18	+65 43 09.95	0.121	Sy1.0	60160633002	0.1	29969	9.11	0.02
MRK 885	16 29 48.38	+67 22 41.98	0.025	Sy1.5	60160641002	0.08	28304	7.27	0.03
MRK 915	22 36 46.50	–12 32 42.89	0.024	Sy1.0	60002060004	1.53	54249	7.13	0.07
MRK 926	23 04 43.48	–08 41 08.62	0.047	Sy1.5	60201029002	1.53	106201	8.37	0.18
Mrk739E	11 36 29.30	+21 35 45.00	0.03	Sy1.0	60260008002	0.12	18547	7.48	0.05
NGC 0985	02 34 37.88	–08 47 17.02	0.043	Sy1.0	60761008002	0.39	21326	8.25	0.05

Table 2 continued

Table 2 (continued)

Source	α_{2000}	δ_{2000}	z	Type	OBSID	Count rate	Exposure	M_{BH}/M_{\odot}	$L_{\text{bol}}/L_{\text{edd}}$
NGC 3227	10 23 30.57	+19 51 54.28	0.004	Sy1.5	60202002002	0.96	49800	6.58	0.05
NGC 3516	11 06 47.46	+72 34 07.29	0.009	Sy1.5	60002042004	0.17	72088	7.11	0.01
NGC 3783	11 39 01.71	-37 44 19.00	0.009	Sy1.0	60101110002	1.11	41265	7.13	0.08
NGC 4051	12 03 09.61	+44 31 52.68	0.002	Sy1.5	60401009002	0.43	311139	5.95	0.02
NGC 4579	12 37 43.52	+11 49 05.49	0.005	Sy1.9	60201051002	0.17	117843	7.8	0.00
NGC 4593	12 39 39.44	-05 20 39.03	0.008	Sy1.0	60001149002	0.63	23317	6.77	0.08
NGC 5273	13 42 08.38	+35 39 15.46	0.004	Sy1.9	60061350002	0.46	21117	6.42	0.03
NGC 5548	14 17 59.54	+25 08 12.60	0.016	Sy1.5	60002044006	0.99	51460	7.97	0.04
NGC 7469	23 03 15.67	+08 52 25.28	0.017	Sy1.2	60101001002	0.75	21579	7.48	0.09
NGC 931	02 28 14.46	+31 18 41.46	0.017	Sy1.0	60101002004	0.74	64242	7.41	0.09
PG0026+129	00 29 13.70	+13 16 03.94	0.142	Sy1.0	60663003002	0.19	147374	7.82	0.85
PG0052+251	00 54 52.11	+25 25 38.98	0.155	Sy1.2	60661001002	0.13	24392	8.7	0.09
PG0804+761	08 10 58.66	+76 02 42.45	0.101	Sy1.0	60160322002	0.18	17315	7.9	0.33
RBS 1037	11 49 18.68	-04 16 50.79	0.085	Sy1.0	60061215002	0.1	40679	8.36	0.04
RBS0295	02 14 37.40	-64 30 05.06	0.074	Sy1.0	60061021002	0.13	23366	8.15	0.07
RBS0770	09 23 43.00	+22 54 32.57	0.033	Sy1.2	60602018002	0.57	42960	7.34	0.27
S52116+81	21 14 01.17	+82 04 48.35	0.084	Sy1.0	60061303002	0.36	18542	8.16	0.23
SDSS J114921.52+532013.4	11 49 21.53	+53 20 13.29	0.095	Sy1.0	60260009002	0.06	24886	8.16	0.01
SDSSJ104326.47+110524.2	10 43 26.47	+11 05 24.26	0.047	Sy1.0	60376004002	0.13	31062	8.01	0.04
SWIFTJ2127.4+5654	21 27 45.39	+56 56 34.91	0.0147	Sy1.0	60001110005	0.712	74578	7.15	0.15
UGC 10120	15 59 09.62	+35 01 47.56	0.031	Sy1.0	60560027002	0.05	62881	—	—
UGC 3478	06 32 47.17	+63 40 25.28	0.013	Sy1.2	60061068002	0.13	21680	—	—
UGC03601	06 55 49.53	+40 00 01.12	0.017	Sy1.5	60160278002	0.1	19674	7.33	0.02
UGC06728	11 45 15.94	+79 40 53.37	0.067	Sy1.2	60160450002	0.14	22615	5.28	51.96
VII ZW 653	16 25 25.95	+85 29 41.69	0.063	Sy1.0	60160639002	0.14	27580	7.46	0.26
VII ZW 742	17 46 59.94	+68 36 39.59	0.063	Sy1.0	60160676004	0.05	31393	7.37	0.10

Table 3. Best-fit parameters obtained from the model $\text{CONST} \times \text{TBABS} \times \text{ZTBABS} \times (\text{XILLVER}/\text{RELXILL}/(\text{RELXILL}+\text{XILLVER}))$ to the source spectra. E_{cut} is in units of KeV.

Source	Γ	E_{cut}	R	χ^2/dof	E_{cut} from the literature	References
1H 0419-577	$1.67^{+0.03}_{-0.04}$	59^{+8}_{-7}	$0.25^{+0.06}_{-0.06}$	1318/1255	83^{+78}_{-31} 63^{+8}_{-9} 49^{+7}_{-5}	Ricci et al. (2017) Turner et al. (2018) Kamraj et al. (2022)
1H1934-063	$2.34^{+0.05}_{-0.06}$	200^{+102}_{-52}	$0.62^{+0.17}_{-0.12}$	1223/1215	≥ 126	Ricci et al. (2017)
2E1739.1-1210	$1.89^{+0.04}_{-0.03}$	>286	$0.57^{+0.29}_{-0.17}$	443/405	≥ 230	Ricci et al. (2017)
2MASS J18302317+731310	$1.44^{+0.05}_{-0.04}$	59^{+14}_{-11}	$0.36^{+0.45}_{-0.20}$	298/280	60^{+49}_{-20}	Akylas, A. & Georgantopoulos, I. (2021)
2MASSJ17485512-3254521	$1.61^{+0.04}_{-0.04}$	75^{+18}_{-14}	<0.59	414/427	159^{+66}_{-55}	Ricci et al. (2017)
2MASSJ04372814-4711298	$1.98^{+0.05}_{-0.05}$	116^{+96}_{-38}	$0.87^{+0.49}_{-0.38}$	272/297	≥ 91 >142	Ricci et al. (2017) Akylas, A. & Georgantopoulos, I. (2021)
2MASXJ11324928+1017473	$2.00^{+0.10}_{-0.10}$	>108	$3.50^{+3.00}_{-1.93}$	63/58	≥ 50	Ricci et al. (2017)
2MASXJ12313717-4758019	$1.88^{+0.06}_{-0.06}$	>112	<0.89	136/178	≥ 231	Ricci et al. (2017)
2MASXJ15295830-1300397	$1.79^{+0.05}_{-0.05}$	>201	<0.60	224/214	≥ 34	Ricci et al. (2017)
2MASXJ1802473-145454	$1.72^{+0.06}_{-0.06}$	133^{+165}_{-52}	$0.32^{+0.09}_{-0.11}$	603/569	≥ 74 66^{+36}_{-18}	Ricci et al. (2017) Akylas, A. & Georgantopoulos, I. (2021)
2MASXJ18470283-7831494	$1.80^{+0.04}_{-0.04}$	122^{+60}_{-36}	$0.59^{+0.49}_{-0.24}$	250/276	≥ 93	Ricci et al. (2017)
2MASXJ18560128+1538059	$1.47^{+0.04}_{-0.04}$	41^{+5}_{-5}	$0.65^{+0.40}_{-0.31}$	287/307	43^{+20}_{-11}	Akylas, A. & Georgantopoulos, I. (2021)
2MASXJ19380437-5109497	$1.85^{+0.05}_{-0.05}$	102^{+64}_{-29}	$0.56^{+0.42}_{-0.34}$	243/255	78^{+191}_{-42} >195	Ricci et al. (2017) Kamraj et al. (2022)
2MASXJ21192912+3332566	$1.80^{+0.04}_{-0.04}$	82^{+33}_{-18}	$0.46^{+0.36}_{-0.27}$	351/344	62^{+150}_{-32}	Ricci et al. (2017)
2MASXJ21355399+4728217	$1.66^{+0.05}_{-0.04}$	56^{+15}_{-10}	<0.89	287/292	89^{+199}_{-38} 67^{+96}_{-23}	Akylas, A. & Georgantopoulos, I. (2021) Ricci et al. (2017)
2MASXJ23013626-5913210	$1.68^{+0.06}_{-0.06}$	41^{+8}_{-6}	$0.68^{+0.62}_{-0.62}$	174/179	55^{+50}_{-19} 31^{+47}_{-13}	Akylas, A. & Georgantopoulos, I. (2021) Ricci et al. (2017)
3C 109	$1.64^{+0.03}_{-0.03}$	72^{+10}_{-9}	$0.33^{+0.21}_{-0.15}$	587/627	59^{+150}_{-26} ≥ 115	Kamraj et al. (2022) Ricci et al. (2017)
3C 111	$1.75^{+0.01}_{-0.01}$	124^{+13}_{-16}	$0.11^{+0.07}_{-0.06}$	910/890	112^{+62}_{-58} ≥ 144	Hinkle & Mushotzky (2021) Ricci et al. (2017)

Table 3 continued

Table 3 (continued)

Source	Γ	E_{cut}	R	χ^2/dof	E_{cut} from the literature	References
3C 120	$1.82^{+0.01}_{-0.01}$	147^{+12}_{-9}	$0.32^{+0.04}_{-0.04}$	1591/1594	136^{+47}_{-29} ≥ 193	Malizia et al. (2014) Ricci et al. (2017)
3C 206	$1.76^{+0.05}_{-0.05}$	112^{+47}_{-33}	<0.59	272/264	158^{+8}_{-7} ≥ 272 >68 >53 >79 ≥ 90 >87	Hinkle & Mushotzky (2021) Ricci et al. (2017) Kang et al. (2020) Kamraj et al. (2022) Akylas, A. & Georgantopoulos, I. (2021) Ricci et al. (2017) Kang et al. (2020)
3C 227	$1.79^{+0.05}_{-0.04}$	>152	<0.24	264/290		
3C 380	$1.66^{+0.06}_{-0.06}$	>217	<0.28	198/178		
3C 382	$1.65^{+0.01}_{-0.01}$	111^{+22}_{-19}	$0.13^{+0.03}_{-0.03}$	1188/1244	158^{+39}_{-76} 133^{+98}_{-40} 215^{+150}_{-60} 166^{+64}_{-37} 130^{+42}_{-32} 120 ± 20	Kamraj et al. (2022) Ezhikode et al. (2020) Tortosa, A. et al. (2018) Ricci et al. (2017) Molina et al. (2019) Tortosa, A. et al. (2018)
3C 390.3	$1.77^{+0.01}_{-0.01}$	144^{+34}_{-19}	$0.21^{+0.07}_{-0.08}$	997/1017		
6dFJ1254564-265702	$1.58^{+0.04}_{-0.05}$	32^{+7}_{-5}	<0.78	164/186	≥ 42	Ricci et al. (2017)
ARK 120	$1.95^{+0.03}_{-0.03}$	346^{+422}_{-133}	$0.51^{+0.10}_{-0.09}$	1147/1146	91^{+100}_{-50} ≥ 292 >763 233^{+147}_{-67}	Akylas, A. & Georgantopoulos, I. (2021) Ricci et al. (2017) Kamraj et al. (2022) Akylas, A. & Georgantopoulos, I. (2021)
Ark 241	$1.88^{+0.05}_{-0.05}$	>115	$0.90^{+0.60}_{-0.47}$	197/214		
ARK 564	$2.41^{+0.04}_{-0.03}$	73^{+30}_{-16}	$0.34^{+0.12}_{-0.07}$	582/574	43^{+3}_{-3}	Kara et al. (2017)
CGCG229-015	$1.71^{+0.08}_{-0.06}$	46^{+14}_{-8}	$0.93^{+0.74}_{-0.56}$	164/173	≥ 38 54^{+76}_{-22} ≥ 23 ≥ 76 ≥ 91 115^{+114}_{-42} ≥ 366	Ricci et al. (2017) Akylas, A. & Georgantopoulos, I. (2021) Ricci et al. (2017) Ricci et al. (2017) Ricci et al. (2017) Kamraj et al. (2022) Ricci et al. (2017)
ESO 025-G002	$1.67^{+0.04}_{-0.04}$	133^{+93}_{-26}	>0.23	385/417		
ESO 031-G008	$2.04^{+0.04}_{-0.04}$	>286	$0.74^{+0.37}_{-0.29}$	305/354		
ESO 209-12	$1.90^{+0.04}_{-0.03}$	>260	$0.38^{+0.24}_{-0.22}$	399/427		
ESO 323-G077	$1.45^{+0.03}_{-0.03}$	89^{+14}_{-13}	$2.40^{+0.85}_{-0.57}$	409/386		
ESO 416-G002	$1.81^{+0.07}_{-0.07}$	>172	$0.31^{+0.47}_{-0.23}$	119/125		

Table 3 continued

Table 3 (continued)

Source	Γ	E_{cut}	R	χ^2/dof	E_{cut} from the literature	References
ESO 511-G030	$1.70^{+0.04}_{-0.04}$	69^{+29}_{-15}	$0.80^{+0.50}_{-0.41}$	308/289	≥ 591	Ricci et al. (2017)
ESO381-G007	$1.66^{+0.07}_{-0.07}$	64^{+35}_{-18}	<1.00	163/161	≥ 76	Ricci et al. (2017)
FAIRALL 1146	$2.03^{+0.03}_{-0.03}$	138^{+73}_{-39}	$1.12^{+0.42}_{-0.35}$	433/423	≥ 72	Ricci et al. (2017)
Fairall 51	$1.53^{+0.33}_{-0.09}$	62^{+115}_{-14}	$4.11^{+1.49}_{-0.62}$	780/762	>166	Kamraj et al. (2022)
GRS 1734-292	$1.67^{+0.02}_{-0.01}$	75^{+6}_{-5}	$0.27^{+0.11}_{-0.06}$	894/923	≥ 105	Ricci et al. (2017)
					84^{+38}_{-26}	Ricci et al. (2017)
					53^{+13}_{-9}	Molina et al. (2019)
					53 ± 10	Tortosa, A. et al. (2018)
H1821+643	$1.91^{+0.03}_{-0.03}$	229^{+221}_{-77}	$0.23^{+0.21}_{-0.19}$	450/454	≥ 130	Ricci et al. (2017)
					114^{+159}_{-44}	Akylas, A. & Georgantopoulos, I. (2021)
HE 1143-1810	$1.79^{+0.07}_{-0.06}$	104^{+24}_{-17}	$0.33^{+0.15}_{-0.14}$	524/617	183^{+219}_{-59}	Ricci et al. (2017)
HE 1136-2304	$1.61^{+0.02}_{-0.02}$	80^{+15}_{-11}	$0.18^{+0.14}_{-0.12}$	648/650	≥ 63	Ricci et al. (2017)
IC 1198	$1.75^{+0.06}_{-0.05}$	124^{+107}_{-43}	$0.96^{+0.68}_{-0.47}$	191/195	97^{+136}_{-77}	Diaz, Y. et al. (2023)
IC 4329A	$1.77^{+0.01}_{-0.01}$	191^{+14}_{-10}	$0.32^{+0.04}_{-0.02}$	2211/2088	—	—
IGR J14471-6414	$2.01^{+0.08}_{-0.08}$	>153	<1.98	115/106	≥ 78	Ricci et al. (2017)
IGRJ14552-5133	$1.93^{+0.02}_{-0.02}$	254^{+194}_{-72}	$0.55^{+0.15}_{-0.15}$	741/775	≥ 59	Ricci et al. (2017)
IGRJ19378-0617	$2.11^{+0.07}_{-0.06}$	228^{+419}_{-83}	$0.75^{+0.35}_{-0.20}$	757/786	≥ 126	Ricci et al. (2017)
					241^{+1377}_{-114}	Kamraj et al. (2022)
IRAS 05589+2828	$1.83^{+0.11}_{-0.09}$	136^{+109}_{-56}	$1.25^{+0.57}_{-0.36}$	843/771	71^{+20}_{-14}	Ricci et al. (2017)
IRAS 09149-6206	$1.69^{+0.14}_{-0.19}$	81^{+60}_{-26}	$0.80^{+0.13}_{-0.11}$	1000/1005	≥ 99	Ricci et al. (2017)
IRAS F12397+3333	$2.34^{+0.04}_{-0.04}$	>97	$0.76^{+0.38}_{-0.36}$	453/399	—	—
IRAS04124-0803	$1.53^{+0.04}_{-0.04}$	80^{+21}_{-14}	$0.52^{+0.27}_{-0.25}$	298/330	≥ 40	Ricci et al. (2017)
IRAS04392-2713	$1.92^{+0.06}_{-0.06}$	>188	$0.46^{+0.20}_{-0.28}$	172/185	≥ 43	Ricci et al. (2017)
KUG 1141+371	$1.92^{+0.11}_{-0.14}$	90^{+27}_{-17}	$0.39^{+0.22}_{-0.19}$	470/514	—	—
MCG-06-30-15	$1.82^{+0.11}_{-0.09}$	126^{+23}_{-19}	$0.98^{+0.66}_{-0.34}$	1574/1516	123^{+101}_{-39}	Ricci et al. (2017)
					170^{+240}_{-53}	Dadina, M. (2007)
					63^{+24}_{-14}	Malizia et al. (2014)
					>110	Tortosa, A. et al. (2018)
MCG+05-40-026	$1.77^{+0.07}_{-0.06}$	104^{+151}_{-41}	<0.96	161/155	—	—

Table 3 continued

Table 3 (continued)

Source	Γ	E_{cut}	R	χ^2/dof	E_{cut} from the literature	References
MCG+08-11-011	$1.83^{+0.01}_{-0.01}$	153^{+15}_{-13}	$0.40^{+0.06}_{-0.05}$	1506/1419	252^{+131}_{-60}	Ricci et al. (2017)
					163^{+53}_{-32}	Molina et al. (2019)
					171^{+44}_{-30}	Malizia et al. (2014)
					175^{+110}_{-50}	Tortosa, A. et al. (2018)
MR 2251-178	$1.63^{+0.01}_{-0.02}$	96^{+17}_{-9}	<0.06	818/859	≥ 59	Ricci et al. (2017)
					132^{+130}_{-68}	Dadina, M. (2007)
					138^{+57}_{-38}	Malizia et al. (2014)
MRK 1040	$1.88^{+0.01}_{-0.01}$	300^{+108}_{-70}	$0.61^{+0.11}_{-0.10}$	1025/1007	≥ 152	Ricci et al. (2017)
					>356	Ezhikode et al. (2020)
					198^{+212}_{-70}	Kamraj et al. (2022)
MRK 1044	$1.80^{+0.05}_{-0.06}$	381^{+553}_{-179}	$0.50^{+0.14}_{-0.11}$	1004/1004	≥ 99	Ricci et al. (2017)
					>120	Akylas, A. & Georgantopoulos, I. (2021)
					≥ 214	Kamraj et al. (2018)
MRK 110	$1.70^{+0.01}_{-0.01}$	92^{+12}_{-10}	$0.12^{+0.02}_{-0.02}$	1624/1576	191^{+207}_{-57}	Ricci et al. (2017)
					117^{+12}_{-17}	Porquet, D. et al. (2021)
MRK 1148	$1.76^{+0.03}_{-0.03}$	99^{+30}_{-20}	<0.22	545/532	≥ 71	Ricci et al. (2017)
					101^{+11}_{-9}	Hinkle & Mushotzky (2021)
MRK 1310	$1.82^{+0.04}_{-0.04}$	>173	$0.28^{+0.31}_{-0.22}$	304/293	≥ 62	Ricci et al. (2017)
MRK 1383	$1.92^{+0.02}_{-0.02}$	>276	$0.98^{+0.21}_{-0.21}$	818/768	—	—
MRK 1392	$1.93^{+0.06}_{-0.05}$	>187	$0.84^{+0.50}_{-0.45}$	185/193	≥ 91	Ricci et al. (2017)
MRK 1393	$1.95^{+0.04}_{-0.04}$	>295	$0.37^{+0.26}_{-0.21}$	352/376	≥ 140	Ricci et al. (2017)
MRK 205	$1.92^{+0.05}_{-0.05}$	131^{+122}_{-45}	$0.60^{+0.44}_{-0.35}$	259/255	≥ 56	Ricci et al. (2017)
					>108	Akylas, A. & Georgantopoulos, I. (2021)
					>365	Kamraj et al. (2018)
MRK 279	$1.49^{+0.04}_{-0.05}$	68^{+18}_{-13}	$0.18^{+0.11}_{-0.12}$	989/994	≥ 125	Ricci et al. (2017)
MRK 290	$1.59^{+0.04}_{-0.04}$	102^{+46}_{-25}	$0.33^{+0.28}_{-0.22}$	316/364	184^{+256}_{-100}	Ricci et al. (2017)
					>53	Ezhikode et al. (2020)
MRK 335	$1.98^{+0.26}_{-0.18}$	>74	$4.52^{+3.73}_{-1.10}$	764/771	≥ 185	Ricci et al. (2017)
MRK 359	$1.91^{+0.03}_{-0.03}$	>163	$0.86^{+0.35}_{-0.31}$	485/433	≥ 40	Ricci et al. (2017)
Mrk 509	$1.77^{+0.02}_{-0.03}$	123^{+17}_{-18}	$0.32^{+0.07}_{-0.07}$	1673/1603	102^{+43}_{-19}	Ricci et al. (2017)

Table 3 continued

Table 3 (continued)

Source	Γ	E_{cut}	R	χ^2/dof	E_{cut} from the literature	References
MRK 590	$1.68^{+0.02}_{-0.02}$	127^{+33}_{-23}	$0.23^{+0.13}_{-0.11}$	818/775	60^{+71}_{-23} ≥ 112	Dadina, M. (2007) Ricci et al. (2017)
MRK 595	$1.31^{+0.18}_{-0.23}$	>35	frozen	104/100	66^{+86}_{-26} 75^{+408}_{-42}	Akylas, A. & Georgantopoulos, I. (2021) Ricci et al. (2017)
MRK 684	$2.14^{+0.09}_{-0.08}$	>150	<2.52	99/103	≥ 127	Ricci et al. (2017)
MRK 704	$1.80^{+0.04}_{-0.04}$	207^{+146}_{-64}	$1.11^{+0.48}_{-0.32}$	374/342	≥ 261	Ricci et al. (2017)
MRK 732	$1.78^{+0.04}_{-0.04}$	>279	$0.20^{+0.27}_{-0.18}$	324/352	81^{+200}_{-40}	Ricci et al. (2017)
MRK 79	$1.86^{+0.05}_{-0.05}$	349^{+516}_{-152}	$0.55^{+0.18}_{-0.15}$	993/968	224^{+366}_{-97} 402^{+165}_{-90}	Ricci et al. (2017) Kamraj et al. (2022)
MRK 813	$1.98^{+0.04}_{-0.04}$	>252	$0.49^{+0.35}_{-0.24}$	345/321	≥ 60	Ricci et al. (2017)
MRK 817	$1.65^{+0.29}_{-0.18}$	>68	$1.64^{+0.39}_{-0.32}$	1013/1007	≥ 242	Ricci et al. (2017)
MRK 841	$1.80^{+0.03}_{-0.03}$	125^{+49}_{-30}	$0.42^{+0.23}_{-0.19}$	467/508	≥ 152 139^{+142}_{-49}	Ricci et al. (2017) Hinkle & Mushotzky (2021)
MRK 876	$1.81^{+0.06}_{-0.06}$	140^{+154}_{-52}	$0.74^{+0.55}_{-0.40}$	193/187	≥ 43	Ricci et al. (2017)
MRK 885	$1.90^{+0.08}_{-0.06}$	>161	$0.56^{+0.83}_{-0.30}$	172/151	≥ 212	Ricci et al. (2017)
MRK 915	$1.72^{+0.03}_{-0.03}$	136^{+68}_{-36}	$0.42^{+0.26}_{-0.22}$	519/547	≥ 79 58^{+11}_{-7}	Ricci et al. (2017) Hinkle & Mushotzky (2021)
MRK 926	$1.70^{+0.02}_{-0.01}$	142^{+33}_{-19}	$0.11^{+0.03}_{-0.02}$	1491/1493	320^{+166}_{-79} 211^{+235}_{-95}	Ricci et al. (2017) Dadina, M. (2007)
Mrk739E	$2.07^{+0.07}_{-0.07}$	>241	$0.84^{+0.43}_{-0.48}$	133/132	≥ 50	Ricci et al. (2017)
NGC 0985	$1.84^{+0.03}_{-0.03}$	>188	$0.42^{+0.21}_{-0.25}$	393/469	≥ 102	Ricci et al. (2017)
NGC 3227	$1.64^{+0.01}_{-0.01}$	94^{+7}_{-6}	$0.62^{+0.10}_{-0.10}$	1224/1163	94^{+16}_{-12} 60^{+5}_{-4} 87^{+16}_{-12}	Ricci et al. (2017) Hinkle & Mushotzky (2021) Kamraj et al. (2022)
NGC 3516	$1.90^{+0.03}_{-0.03}$	>448	$1.27^{+0.29}_{-0.14}$	696/655	132^{+87}_{-43}	Ricci et al. (2017)
NGC 3783	$1.55^{+0.07}_{-0.03}$	112^{+24}_{-19}	$0.90^{+0.11}_{-0.12}$	1137/1145	77^{+16}_{-11} 98^{+79}_{-34}	Kamraj et al. (2022) Fabian et al. (2015)
NGC 4051	$1.78^{+0.07}_{-0.07}$	>452	$1.33^{+1.02}_{-0.67}$	1674/1647	59^{+25}_{-13}	Ricci et al. (2017)
NGC 4579	$1.73^{+0.06}_{-0.06}$	82^{+49}_{-23}	$0.29^{+0.09}_{-0.07}$	819/739	—	—
NGC 4593	$1.87^{+0.02}_{-0.02}$	>648	$0.57^{+0.26}_{-0.13}$	523/571	≥ 655	Ricci et al. (2017)

Table 3 continued

Table 3 (continued)

Source	Γ	E_{cut}	R	χ^2/dof	E_{cut} from the literature	References
NGC 5273	$1.46^{+0.06}_{-0.06}$	68^{+25}_{-16}	$1.03^{+0.33}_{-0.28}$	593/574	≥ 294 115^{+91}_{-37}	Ricci et al. (2017) Akylas, A. & Georgantopoulos, I. (2021)
NGC 5548	$1.71^{+0.03}_{-0.01}$	118^{+12}_{-8}	$0.48^{+0.10}_{-0.06}$	1219/1143	≥ 281 70^{+40}_{-10}	Kamraj et al. (2022) Ricci et al. (2017) Ursini, F. et al. (2015)
NGC 7469	$1.95^{+0.02}_{-0.02}$	122^{+27}_{-21}	$0.77^{+0.19}_{-0.18}$	647/692	≥ 316 113^{+33}_{-22}	Ricci et al. (2017) Hinkle & Mushotzky (2021)
NGC 931	$1.88^{+0.01}_{-0.01}$	229^{+78}_{-42}	$0.63^{+0.12}_{-0.12}$	974/954	≥ 152	Ricci et al. (2017)
PG0026+129	$1.82^{+0.02}_{-0.02}$	110^{+20}_{-15}	$0.34^{+0.12}_{-0.11}$	903/856	≥ 45	Ricci et al. (2017)
PG0052+251	$1.66^{+0.02}_{-0.01}$	>76	<0.18	167/190	≥ 137	Ricci et al. (2017)
PG0804+761	$1.94^{+0.05}_{-0.05}$	>269	$0.71^{+0.49}_{-0.35}$	217/221	≥ 67	Ricci et al. (2017)
RBS 1037	$2.00^{+0.06}_{-0.06}$	>133	$1.04^{+0.28}_{-0.30}$	208/200	≥ 34	Ricci et al. (2017)
RBS0295	$1.73^{+0.06}_{-0.05}$	>91	<0.42	212/218	—	—
RBS0770	$1.65^{+0.07}_{-0.04}$	59^{+18}_{-12}	$0.57^{+0.22}_{-0.18}$	755/713	≥ 256	Ricci et al. (2017)
S52116+81	$1.75^{+0.04}_{-0.04}$	103^{+40}_{-24}	$0.37^{+0.27}_{-0.22}$	370/409	≥ 267 ≥ 175	Kamraj et al. (2018) Ricci et al. (2017)
SDSS J114921.52+532013.4	$1.53^{+0.10}_{-0.10}$	29^{+9}_{-7}	<2.02	88/75	>93 47^{+86}_{-14}	Molina et al. (2019) Ricci et al. (2017)
SDSSJ104326.47+110524.2	$1.72^{+0.05}_{-0.05}$	>123	<0.43	220/236	≥ 91	Ricci et al. (2017)
SWIFTJ2127.4+5654	$1.89^{+0.01}_{-0.01}$	84^{+6}_{-6}	$0.75^{+0.10}_{-0.09}$	1094/1089	62^{+25}_{-15} 92^{+26}_{-17}	Ricci et al. (2017) Kang et al. (2021)
UGC 10120	$1.91^{+0.07}_{-0.06}$	>225	<0.71	185/192	—	—
UGC 3478	$1.99^{+0.06}_{-0.06}$	>98	<1.07	212/196	—	—
UGC03601	$1.49^{+0.09}_{-0.08}$	58^{+45}_{-19}	<0.86	127/109	74^{+240}_{-32}	Ricci et al. (2017)
UGC06728	$1.62^{+0.05}_{-0.05}$	66^{+20}_{-14}	$0.55^{+0.43}_{-0.32}$	223/241	73^{+31}_{-19} 63^{+133}_{-25}	Ricci et al. (2017) Kamraj et al. (2022)
VII ZW 653	$2.05^{+0.05}_{-0.05}$	>114	$1.10^{+0.61}_{-0.51}$	187/213	—	—
VII ZW 742	$1.88^{+0.08}_{-0.08}$	>174	$1.25^{+1.04}_{-0.71}$	99/108	≥ 52	Ricci et al. (2017)

Table 4. Best-fit parameters obtained from the model $\text{CONST} \times \text{TBABS} \times \text{zTBABS} \times (\text{XILLVERCP}/\text{RELXILLCP}/(\text{RELXILLCP}+\text{XILLVERCP}))$ to the source spectra. $N_{\text{H}}^{\text{INT}}$ is the host galaxy hydrogen column density in units of 10^{22} atoms cm^{-2} , kT_{e} is in units of KeV, the model normalization is in units of 10^{-4} photons $\text{keV}^{-1} \text{cm}^{-2} \text{s}^{-1}$.

Source	$N_{\text{H}}^{\text{INT}}$	Γ	kT_{e}	R	$N_{\text{relkillCP}}$	$N_{\text{xillverCP}}$	χ^2/dof
1H 0419-577	$1.95^{+0.36}_{-0.36}$	$1.82^{+0.01}_{-0.01}$	14^{+1}_{-1}	$0.15^{+0.06}_{-0.06}$	—	$0.79^{+0.01}_{-0.01}$	1321/1255
1H1934-063	—	$2.14^{+0.03}_{-0.03}$	>53	$0.62^{+0.16}_{-0.12}$	$0.97^{+0.13}_{-0.13}$	—	1221/1215
2MASS J1830231+731310	—	$1.64^{+0.03}_{-0.03}$	17^{+22}_{-4}	<0.55	—	$0.31^{+0.01}_{-0.01}$	307/280
2MASSJ17485512-3254521	—	$1.74^{+0.03}_{-0.03}$	>15	<0.43	—	$0.68^{+0.02}_{-0.02}$	420/427
2MASXJ04372814-4711298	—	$2.03^{+0.04}_{-0.04}$	>16	$0.90^{+0.50}_{-0.41}$	—	$0.18^{+0.01}_{-0.01}$	271/297
2MASXJ1802473-145454	—	$1.79^{+0.03}_{-0.04}$	29^{+60}_{-11}	$0.27^{+0.13}_{-0.10}$	$1.11^{+0.18}_{-0.12}$	—	604/569
2MASXJ18470283-7831494	—	$1.87^{+0.04}_{-0.04}$	>17	<0.95	—	$0.44^{+0.02}_{-0.02}$	194/263
2MASXJ18560128+1538059	—	$1.72^{+0.03}_{-0.03}$	13^{+3}_{-2}	$0.49^{+0.40}_{-0.41}$	—	$0.49^{+0.01}_{-0.01}$	295/307
2MASXJ19380437-5109497	—	$1.93^{+0.04}_{-0.04}$	>17	<0.95	—	$0.43^{+0.02}_{-0.02}$	244/255
2MASXJ21192912+3332566	—	$1.90^{+0.03}_{-0.03}$	>15	$0.38^{+0.36}_{-0.27}$	—	$0.45^{+0.01}_{-0.01}$	354/344
2MASXJ21355399+4728217	—	$1.81^{+0.03}_{-0.03}$	16^{+12}_{-4}	$0.40^{+0.36}_{-0.35}$	—	$0.43^{+0.02}_{-0.02}$	291/292
2MASXJ23013626-5913210	—	$1.87^{+0.04}_{-0.04}$	13^{+6}_{-3}	$0.52^{+0.65}_{-0.42}$	—	$0.30^{+0.02}_{-0.02}$	176/179
3C 109	—	$1.78^{+0.02}_{-0.02}$	18^{+8}_{-3}	$0.26^{+0.17}_{-0.16}$	—	$0.32^{+0.01}_{-0.01}$	591/627
3C 111	$2.46^{+0.39}_{-0.38}$	$1.84^{+0.01}_{-0.01}$	37^{+34}_{-10}	$0.07^{+0.07}_{-0.06}$	—	$2.46^{+0.03}_{-0.03}$	1081/1025
3C 120	—	$1.85^{+0.01}_{-0.01}$	45^{+19}_{-8}	$0.23^{+0.04}_{-0.04}$	$2.72^{+0.11}_{-0.08}$	—	1566/1592
3C 206	—	$1.84^{+0.04}_{-0.04}$	>15	<0.52	—	$0.63^{+0.02}_{-0.02}$	271/264
3C 382	—	$1.77^{+0.01}_{-0.01}$	34^{+18}_{-8}	$0.07^{+0.05}_{-0.05}$	$1.73^{+0.02}_{-0.02}$	—	1276/1247
3C 390.3	$2.55^{+0.41}_{-0.41}$	$1.85^{+0.01}_{-0.01}$	44^{+49}_{-12}	$0.17^{+0.08}_{-0.08}$	—	$2.44^{+0.03}_{-0.03}$	1002/1017
6dFJ1254564-265702	—	$1.69^{+0.05}_{-0.04}$	9^{+2}_{-2}	<1.09	—	$0.23^{+0.01}_{-0.01}$	121/143
ARK 120	—	$1.96^{+0.02}_{-0.02}$	>67	$0.50^{+0.09}_{-0.07}$	$2.27^{+0.06}_{-0.12}$	—	1147/1145
ARK 564	—	$2.40^{+0.02}_{-0.02}$	24^{+10}_{-6}	$0.46^{+0.29}_{-0.07}$	$0.96^{+0.10}_{-0.26}$	<0.08	1168/1165
CGCG229-015	—	$1.89^{+0.05}_{-0.04}$	17^{+42}_{-6}	$0.82^{+0.83}_{-0.55}$	—	$0.21^{+0.01}_{-0.01}$	168/173
ESO 025-G002	—	$1.74^{+0.03}_{-0.03}$	>22	<0.25	—	$0.69^{+0.02}_{-0.02}$	389/417
ESO 323-G077	38^{+3}_{-3}	$1.70^{+0.02}_{-0.02}$	35^{+13}_{-12}	$2.35^{+0.81}_{-0.66}$	—	$0.29^{+0.02}_{-0.02}$	411/386
ESO 511-G030	—	$1.81^{+0.04}_{-0.03}$	>16	$0.57^{+0.55}_{-0.32}$	—	$0.22^{+0.01}_{-0.01}$	313/289

Table 4 continued

Table 4 (continued)

Source	$N_{\text{H}}^{\text{INT}}$	Γ	kT_{e}	R	$N_{\text{relkillCP}}$	$N_{\text{xillverCP}}$	χ^2/dof
ESO381-G007	—	$1.80^{+0.05}_{-0.05}$	>12	<0.77	—	$0.25^{+0.01}_{-0.01}$	165/161
FAIR-ALL 1146	—	$2.05^{+0.03}_{-0.03}$	>25	$1.06^{+0.53}_{-0.31}$	—	$0.69^{+0.02}_{-0.02}$	434/423
Fairall 51	$11.55^{+1.60}_{-1.23}$	$2.00^{+0.09}_{-0.17}$	>34	$4.42^{+1.38}_{-1.04}$	$0.39^{+0.05}_{-0.05}$	—	786/761
GRS 1734-292	$3.75^{+0.46}_{-0.44}$	$1.81^{+0.01}_{-0.01}$	20^{+4}_{-2}	$0.24^{+0.08}_{-0.09}$	—	$2.98^{+0.05}_{-0.04}$	818/856
H1821+643	—	$1.94^{+0.03}_{-0.03}$	>39	$0.21^{+0.21}_{-0.17}$	—	$1.04^{+0.03}_{-0.03}$	451/454
HE 1143-1810	—	$1.85^{+0.02}_{-0.02}$	27^{+19}_{-7}	$0.26^{+0.15}_{-0.13}$	—	$1.37^{+0.02}_{-0.02}$	534/597
HE1136-2304	—	$1.73^{+0.02}_{-0.02}$	18^{+7}_{-3}	<0.24	—	$0.40^{+0.01}_{-0.01}$	656/650
IC 1198	—	$1.83^{+0.04}_{-0.04}$	>18	$0.91^{+0.75}_{-0.47}$	—	$0.21^{+0.01}_{-0.01}$	193/195
IC 4329A	$1.89^{+0.11}_{-0.12}$	$1.83^{+0.003}_{-0.003}$	64^{+15}_{-12}	$0.30^{+0.03}_{-0.03}$	—	$6.27^{+0.03}_{-0.04}$	2245/2088
IGRJ14552-5133	—	$1.96^{+0.02}_{-0.02}$	>45	$0.53^{+0.15}_{-0.13}$	—	$0.50^{+0.01}_{-0.01}$	741/775
IGRJ19378-0617	—	$2.13^{+0.05}_{-0.05}$	>46	$0.74^{+0.33}_{-0.19}$	$0.91^{+0.17}_{-0.19}$	—	757/786
IRAS 05589+2828	—	$1.90^{+0.11}_{-0.07}$	43^{+120}_{-24}	$1.00^{+1.03}_{-0.40}$	$1.19^{+0.14}_{-0.27}$	—	788/738
IRAS 09149-6206	—	$1.90^{+0.10}_{-0.08}$	18^{+21}_{-4}	$2.05^{+0.68}_{-0.47}$	$0.60^{+0.02}_{-0.02}$	—	992/1005
IRAS04124-0803	—	$1.67^{+0.03}_{-0.03}$	15^{+4}_{-3}	$0.39^{+0.27}_{-0.23}$	—	$0.58^{+0.02}_{-0.02}$	292/330
KUG 1141+371	—	$1.92^{+0.02}_{-0.02}$	29^{+79}_{-11}	$0.33^{+0.22}_{-0.18}$	—	$0.58^{+0.01}_{-0.01}$	517/547
MCG-06-30-15	—	$1.97^{+0.06}_{-0.04}$	50^{+98}_{-11}	$0.58^{+0.39}_{-0.12}$	$1.71^{+0.31}_{-0.47}$	$0.89^{+0.19}_{-0.18}$	1572/1517
MCG+05-40-026	—	$1.84^{+0.06}_{-0.06}$	>16	<0.78	—	$0.27^{+0.02}_{-0.01}$	162/155
MCG+08-11-011	—	$1.88^{+0.01}_{-0.01}$	56^{+26}_{-16}	$0.35^{+0.06}_{-0.05}$	$2.92^{+0.02}_{-0.02}$	—	1506/1419
MR 2251-178	—	$1.76^{+0.01}_{-0.01}$	22^{+8}_{-4}	<0.02	—	$2.59^{+0.02}_{-0.02}$	835/859
MRK 1040	—	$1.91^{+0.01}_{-0.01}$	>62	$0.60^{+0.12}_{-0.10}$	—	$1.48^{+0.02}_{-0.02}$	1029/1007
MRK 1044	—	$2.15^{+0.03}_{-0.05}$	>96	$0.53^{+0.16}_{-0.15}$	$0.63^{+0.16}_{-0.15}$	$0.19^{+0.10}_{-0.11}$	1388/1286
MRK 110	—	$1.82^{+0.01}_{-0.01}$	25^{+4}_{-3}	<0.09	$2.03^{+0.01}_{-0.01}$	—	1630/1576
MRK 1148	—	$1.85^{+0.02}_{-0.02}$	25^{+74}_{-8}	<0.17	—	$1.04^{+0.02}_{-0.02}$	555/532
MRK 205	—	$1.97^{+0.04}_{-0.04}$	>20	$0.57^{+0.43}_{-0.35}$	—	$0.47^{+0.02}_{-0.02}$	260/255
MRK 279	—	$1.68^{+0.01}_{-0.01}$	15^{+2}_{-2}	$0.13^{+0.09}_{-0.08}$	$0.29^{+0.02}_{-0.01}$	$0.09^{+0.02}_{-0.02}$	1007/995
MRK 290	—	$1.70^{+0.03}_{-0.03}$	>15	<0.51	—	$0.43^{+0.01}_{-0.01}$	319/364
Mrk 509	—	$1.82^{+0.02}_{-0.01}$	23^{+3}_{-2}	$0.19^{+0.03}_{-0.04}$	$2.15^{+0.05}_{-0.04}$	—	1691/1603
MRK 590	$2.07^{+0.59}_{-0.57}$	$1.82^{+0.03}_{-0.03}$	>49	$0.20^{+0.12}_{-0.11}$	$0.92^{+0.19}_{-0.16}$	—	815/774
MRK 704	$10.24^{+1.38}_{-1.36}$	$1.86^{+0.03}_{-0.03}$	>30	$1.11^{+0.50}_{-0.37}$	—	$0.62^{+0.04}_{-0.03}$	374/342
MRK 79	—	$1.88^{+0.04}_{-0.04}$	>47	$0.53^{+0.19}_{-0.16}$	$1.26^{+0.06}_{-0.13}$	—	994/968

Table 4 continued

Table 4 (continued)

Source	$N_{\text{H}}^{\text{INT}}$	Γ	kT_{e}	R	$N_{\text{relkillCP}}$	$N_{\text{xillverCP}}$	χ^2/dof
MRK 841	—	$1.86^{+0.02}_{-0.02}$	33^{+185}_{-14}	$0.37^{+0.23}_{-0.19}$	—	$0.89^{+0.02}_{-0.02}$	469/508
MRK 876	—	$1.86^{+0.05}_{-0.04}$	>15	$0.70^{+0.56}_{-0.39}$	—	$0.18^{+0.01}_{-0.01}$	192/187
MRK 915	$6.90^{+0.98}_{-1.04}$	$1.81^{+0.03}_{-0.03}$	>28	$0.33^{+0.25}_{-0.16}$	—	$0.45^{+0.01}_{-0.02}$	522/547
MRK 926	—	$1.78^{+0.01}_{-0.01}$	31^{+7}_{-5}	$0.10^{+0.02}_{-0.02}$	$3.13^{+0.11}_{-0.09}$	—	1525/1494
NGC 3227	$2.66^{+0.34}_{-0.33}$	$1.76^{+0.01}_{-0.01}$	26^{+6}_{-4}	$0.56^{+0.09}_{-0.09}$	—	$1.89^{+0.02}_{-0.02}$	1198/1163
NGC 3783	—	$1.74^{+0.02}_{-0.02}$	48^{+48}_{-9}	$0.41^{+0.20}_{-0.16}$	$2.33^{+0.23}_{-0.15}$	$0.76^{+0.27}_{-0.26}$	1270/1132
NGC 4579	—	$1.84^{+0.03}_{-0.03}$	23^{+23}_{-7}	$0.25^{+0.09}_{-0.07}$	$0.33^{+0.04}_{-0.03}$	—	828/739
NGC 5273	—	$1.79^{+0.06}_{-0.10}$	>18	$0.98^{+0.53}_{-0.33}$	$1.06^{+0.21}_{-0.20}$	—	589/572
NGC 5548	$3.32^{+0.34}_{-0.35}$	$1.81^{+0.01}_{-0.01}$	35^{+9}_{-7}	$0.43^{+0.10}_{-0.09}$	—	$2.23^{+0.07}_{-0.03}$	1228/1143
NGC 7469	—	$2.00^{+0.02}_{-0.02}$	45^{+52}_{-17}	$0.74^{+0.20}_{-0.17}$	—	$1.59^{+0.03}_{-0.03}$	650/692
NGC 931	—	$1.91^{+0.01}_{-0.01}$	>50	$0.58^{+0.14}_{-0.09}$	—	$1.40^{+0.02}_{-0.02}$	979/954
PG0026+129	—	$1.89^{+0.01}_{-0.01}$	22^{+9}_{-4}	$0.30^{+0.12}_{-0.11}$	—	$0.39^{+0.12}_{-0.11}$	899/856
RBS0770	—	$1.78^{+0.02}_{-0.02}$	15^{+3}_{-2}	$0.42^{+0.16}_{-0.13}$	$0.75^{+0.04}_{-0.04}$	—	757/713
S52116+81	—	$1.84^{+0.03}_{-0.03}$	>18	$0.29^{+0.26}_{-0.20}$	—	$0.74^{+0.02}_{-0.02}$	373/409
SDSS J114921.52+532013.4	—	$1.70^{+0.07}_{-0.07}$	7^{+1}_{-1}	$1.38^{+3.34}_{-1.26}$	—	$0.08^{+0.01}_{-0.01}$	88/75
SWIFTJ2127.4+5654	—	$1.96^{+0.01}_{-0.01}$	21^{+3}_{-2}	$0.72^{+0.10}_{-0.10}$	—	$1.49^{+0.01}_{-0.01}$	1084/1089
UGC03601	—	$1.68^{+0.07}_{-0.06}$	>9	<0.53	—	$0.24^{+0.01}_{-0.01}$	129/109
UGC06728	—	$1.73^{+0.07}_{-0.07}$	17^{+25}_{-5}	$0.34^{+0.42}_{-0.21}$	$0.31^{+0.58}_{-0.39}$	—	223/239

B. kT_e : THE TEMPERATURE OF THE CORONA

Here, we discuss the results obtained from the spectral analysis using the model $\text{CONST} \times \text{TBABS} \times \text{ZTBABS} \times (\text{XILLVERCP}/\text{RELXILLCP}/(\text{RELXILLCP}+\text{XILLVERCP}))$.

We also compare the best-fit values of our analysis with the previously measured values of kT_e from the literature, if available. Among the 42 sources for which we could constrain kT_e , 18 sources were already discussed by us earlier (Pal et al. 2022; Pal & Stalin 2023). Therefore, here we give details on the rest of the 24 sources.

2MASXJ23013626-5913210: This source at a redshift $z = 0.150$ was observed by *NuSTAR* once in 2017. We used Model–2a to estimate the coronal properties of the source. We found the source spectra to be well described with $\Gamma = 1.87_{-0.04}^{+0.04}$ and $kT_e = 13.35_{-0.48}^{+0.23}$ keV. Previously, using similar Comptonization model Kamraj et al. (2022) found a value of $\Gamma = 1.78_{-0.11}^{+0.14}$ and $kT_e = 11.10_{-0.87}^{+12.22}$ keV. Our results are thus in agreement with Kamraj et al. (2022).

3C 120: This is a radio-loud Seyfert 1 galaxy at $z=0.033$. *NuSTAR* observed the source twice on the same day in February 2013. Of the two observations, we analysed the spectrum with the highest exposure time using Model–2b. We obtained values of $\Gamma = 1.85_{-0.01}^{+0.01}$ and $kT_e = 45.31_{-0.82}^{+18.79}$ keV. Analysing the same data set using *relxillCP* Kang & Wang (2022) found a lower limit of $kT_e > 91$ keV.

3C 390.3: This radio-loud Seyfert 1 galaxy at $z=0.05613$ was observed twice by *NuSTAR* on the same day in May 2013. From spectral analysis of the data using Model–2a we obtained $\Gamma = 1.84_{-0.01}^{+0.01}$ and $kT_e = 44.13_{-12.50}^{+54.75}$ keV. For the same data set Kang & Wang (2022) and Kamraj et al. (2022) reported lower limits of $kT_e > 46$ keV and $kT_e > 49.86$ keV respectively.

ARK 564: This source was observed by *NuSTAR* three times between May 2015 and November 2018. Of these, results on the observation done by *NuSTAR* in September 2018 is reported in this work for the first time. Fitting the observed data with Model–2c, we obtained $\Gamma = 2.40_{-0.02}^{+0.02}$ and $kT_e = 24.28_{-0.29}^{+13.60}$ keV respectively. From analysis of the data acquired by *NuSTAR* in 2015, Kara et al. (2017) determined $kT_e = 15 \pm 2$ keV arguing the source to have the coolest corona. Also, based on two epochs of data, Barua et al. (2020) reported variation in the temperature of the corona.

HE 1136–2304: Active Galactic Nuclei exhibit flux variations across various timescales and across the entire electromagnetic spectrum. In the last decade, an increasing number of sources have displayed notably more pronounced changes in their flux and spectral character-

istics, both in the X-ray range and the optical/UV range. These events are often referred to as changing-look AGN (Ricci & Trakhtenbrot 2022). HE 1136–2304 is such a changing look AGN. It was found to change its optical spectral nature from Type 2 in 1993 to Type 1.5 in 2014 (Parker et al. 2016). It was observed by *NuSTAR* twice on the same day in July 2014. Of the two, we analysed the spectrum with maximum exposure. The best-fit values obtained from fitting Model–2a to the source spectrum were $\Gamma = 1.78_{-0.02}^{+0.03}$ and $kT_e = 27.81_{-0.30}^{+78.85}$ keV. From an analysis of same *NuSTAR* spectrum using *relxillCP* Kang & Wang (2022) obtained a lower limit of $kT_e > 21$ keV.

IC 4329A: This Seyfert 1 galaxy was observed six times by *NuSTAR*, once in 2012 and the others during August 2021. We analysed here the *NuSTAR* spectrum taken in 2012. Fitting the spectrum using Model–2a we obtained best-fit values of Γ and kT_e as $1.83_{-0.003}^{+0.003}$ and $64.16_{-11.63}^{+15.41}$ keV respectively. This source has been studied extensively in the past. For example, Tortosa, A. et al. (2018) reported $kT_e = 37 \pm 7$ keV from fitting *compTT* for a slab geometry. Kang & Wang (2022) estimated $kT_e = 71_{-15}^{+37}$ keV using *relxillCP* model. Kamraj et al. (2022) also found $kT_e = 82_{-7}^{+16}$ keV from *xillverCP* fit to the source spectrum.

2MASXJ21355399+4728217: This Seyfert galaxy was observed by *NuSTAR* on September 2019. From the analysis of the source spectrum Akylas, A. & Georgantopoulos, I. (2021) reported $E_{\text{cut}} = 55_{-19}^{+50}$ keV. We analysed the same observation ID using Model–2a and found $kT_e = 15.57_{-0.90}^{+12.24}$ keV.

IRAS 04124-0803: Analysis of the *NuSTAR* observations (done in September 2021) on this source is carried out for the first time. From fitting Model–2a to the source spectrum, we obtained best-fit values of $\Gamma = 1.66_{-0.03}^{+0.03}$ and $kT_e = 14.88_{-0.57}^{+0.70}$ keV.

IRAS 09149-6206: Results on *NuSTAR* observations of this source are reported for the first time. This source was observed by *NuSTAR* twice between July and August, 2018. We modelled the Comptonized spectrum (observed on August 2018) and estimated the best-fit value of kT_e using Model–2b. From the model fit to the spectrum we obtained $\Gamma = 1.90_{-0.09}^{+0.11}$ and $kT_e = 18.09_{-0.07}^{+16.87}$ keV.

IRAS 05589+2828: This Seyfert 1 galaxy situated at $z=0.02940$ was observed by *NuSTAR* in April 2020. The temperature of the corona of the source is reported for the first time. From the physical model fit to the observed spectrum, we found values of $\Gamma = 1.90_{-0.07}^{+0.11}$ and $kT_e = 42.90_{-23.92}^{+120.46}$ keV.

Mrk 1148: This Seyfert 1 galaxy was observed by *NuSTAR* in January, 2018. We carried out the spectral anal-

ysis using Model–2a. The best-fit values obtained using the model fit to the spectrum are $\Gamma = 1.86_{-0.02}^{+0.02}$ and $kT_e = 24.04_{-06.76}^{+19.81}$ keV. Recently, analysing the same spectrum, both Kamraj et al. (2022) and Kang & Wang (2022) found values of $kT_e > 18$ keV.

Mrk 509: *NuSTAR* observed this source two times between April and June 2015. In this work, we analysed the spectrum taken on April 2015. From fitting Model–2c to the observed spectrum we obtained $\Gamma = 1.86_{-0.02}^{+0.01}$ and $kT_e = 35.78_{-05.72}^{+06.78}$ keV. On analysis of the same spectrum using *relxillCP* model Kang & Wang (2022) reported $kT_e = 24 \pm 2$ keV.

2MASXJ18560128+1538059: This Seyfert 1 galaxy was observed by *NuSTAR* in 2017, and from the analysis of the source spectrum using our Model–2a, we found $kT_e = 12.32_{-2.36}^{+3.12}$ keV. Using the same observation ID Akylas, A. & Georgantopoulos, I. (2021) reported $E_{\text{cut}} = 43_{-11}^{+20}$ keV.

PG 0026+129: *NuSTAR* observed the Seyfert 1 galaxy once in January 2021 and results on the analysis of the observation is reported for the first time. From Model–2a fit to the observed spectrum we obtained best-fit values of $\Gamma = 1.89_{-0.01}^{+0.01}$ and $kT_e = 22.18_{-04.03}^{+08.88}$ keV.

SWIFTJ2127.4+5654: This source classified as a narrow line Seyfert 1 galaxy, was observed by *NuSTAR* nine times between September 2012 and December 2018. We analysed the observations carried out by *NuSTAR* in September 2012 as it has the maximum exposure time. By fitting the observed spectrum using Model–2a, we obtained $\Gamma = 1.96_{-0.01}^{+0.01}$ and $kT_e = 20.70_{-01.94}^{+03.36}$ keV. From an analysis of the same spectrum, Kang et al. (2021) reported a kT_e of 21_{-2}^{+2} keV.

IGRJ19378–0617: This source is situated at $z=0.0103$. It was classified as a Seyfert 1 galaxy, observed six times by *NuSTAR* between 2015 and 2022. From fitting the source spectrum using Model–2a, we found $kT_e = 49.35_{-13.04}^{+36.94}$ keV. From the spectral analysis of the source spectrum Kamraj et al. (2022) reported $kT_e > 122$ keV.

Fairall 51: *NuSTAR* observed this Seyfert 1 galaxy 4 times between 2018 and 2021. We analysed the *NuSTAR*

spectrum observed in June 2018. From fitting the source spectrum using Model–2a, we found $kT_e = 19.48_{-1.83}^{+6.54}$ keV.

Mrk 279: This Seyfert 1 galaxy was observed 4 times by *NuSTAR* between 2019 and 2020. We analysed the August 2020 spectrum using Model–2c and found $kT_e = 16.38_{-1.55}^{+1.72}$ keV. By analysing the source spectrum taken in October 2019, Kang & Wang (2022) reported a lower limit of $kT_e > 84$ keV.

ESO 323–G077: This source is classified as a Seyfert 1.5 galaxy (Winkler 1992), situated at $z = 0.0155$. *NuSTAR* observed this source six times between August 2016 to February 2017. We analyzed January 2017 *NuSTAR* data. From the Model–2a fit to the source spectrum, we obtained $kT_e = 35.21_{-11.89}^{+13.02}$ keV. For this source, Kamraj et al. (2022) reported a lower limit of $kT_e > 34$ keV.

3C 109: This Seyfert galaxy was observed by *NuSTAR* twice in August 2017. We analysed the one with the maximum exposure time. By fitting Model–2a to the source spectrum, we found $kT_e = 18.09_{-2.72}^{+6.91}$ keV.

RBS0770: This source was observed four times between 2012 and 2021 by *NuSTAR*. By fitting Model–2a to the source spectrum we found $kT_e = 17.71_{-2.38}^{+4.30}$ keV. From the analysis of the same observation, Kamraj et al. (2022) reported a lower limit for $kT_e > 24$ keV.

CGCG229–015: This nearby Seyfert 1 galaxy was observed once by *NuSTAR* on February 2018. From an analysis of the same observation ID Akylas, A. & Georgantopoulos, I. (2021) reported $E_{\text{cut}} = 54_{-11.89}^{+13.02}$ keV. From the Model–2a fit to the source spectrum, we obtained $kT_e = 17.00_{-5.61}^{+41.62}$ keV.

3C 382: This Seyfert galaxy was observed 7 times between 2012 and 2016. We analysed the 2013 spectrum and reported $kT_e = 33.07_{-7.76}^{+16.81}$ keV. From the analysis of the same observation Ezhikode et al. (2020) reported $E_{\text{cut}} = 132.75_{-39.98}^{+98.32}$ keV.

SDSS J114921.52+532013.4: This Seyfert 1 galaxy was observed once in 2016. From the Model–2a fit to the source spectrum, we found $kT_e = 6.50_{-0.97}^{+1.25}$ keV.

REFERENCES

- Abramowicz, M. A., Czerny, B., Lasota, J. P., & Szuszkiewicz, E. 1988, *ApJ*, 332, 646, doi: [10.1086/166683](https://doi.org/10.1086/166683)
- Akylas, A., & Georgantopoulos, I. 2021, *A&A*, 655, A60, doi: [10.1051/0004-6361/202141186](https://doi.org/10.1051/0004-6361/202141186)
- Arnaud, K. A. 1996, *Astronomical Society of the Pacific Conference Series*, Vol. 101, *XSPEC: The First Ten Years*, ed. G. H. Jacoby & J. Barnes, 17
- Ballantyne, D. R., Bollenbacher, J. M., Brenneman, L. W., et al. 2014, *ApJ*, 794, 62, doi: [10.1088/0004-637X/794/1/62](https://doi.org/10.1088/0004-637X/794/1/62)
- Baloković, M., Harrison, F. A., Madejski, G., et al. 2020, *ApJ*, 905, 41, doi: [10.3847/1538-4357/abc342](https://doi.org/10.3847/1538-4357/abc342)
- Barua, S., Jithesh, V., Misra, R., et al. 2020, *MNRAS*, 492, 3041, doi: [10.1093/mnras/staa067](https://doi.org/10.1093/mnras/staa067)

- . 2021, *ApJ*, 921, 46, doi: [10.3847/1538-4357/ac1c74](https://doi.org/10.3847/1538-4357/ac1c74)
- Beloborodov, A. M. 1999, *ApJL*, 510, L123, doi: [10.1086/311810](https://doi.org/10.1086/311810)
- Boissay, Rozenn, Ricci, Claudio, & Paltani, Stéphane. 2016, *A&A*, 588, A70, doi: [10.1051/0004-6361/201526982](https://doi.org/10.1051/0004-6361/201526982)
- Brandt, W. N., Mathur, S., & Elvis, M. 1997, *MNRAS*, 285, L25, doi: [10.1093/mnras/285.3.L25](https://doi.org/10.1093/mnras/285.3.L25)
- Brightman, M., Silverman, J. D., Mainieri, V., et al. 2013, *MNRAS*, 433, 2485, doi: [10.1093/mnras/stt920](https://doi.org/10.1093/mnras/stt920)
- Brightman, M., Masini, A., Ballantyne, D. R., et al. 2016, *The Astrophysical Journal*, 826, 93, doi: [10.3847/0004-637X/826/1/93](https://doi.org/10.3847/0004-637X/826/1/93)
- Dadina, M. 2007, *A&A*, 461, 1209, doi: [10.1051/0004-6361:20065734](https://doi.org/10.1051/0004-6361:20065734)
- . 2008, *A&A*, 485, 417, doi: [10.1051/0004-6361:20077569](https://doi.org/10.1051/0004-6361:20077569)
- Denney, K. D., Watson, L. C., Peterson, B. M., et al. 2009, *ApJ*, 702, 1353, doi: [10.1088/0004-637X/702/2/1353](https://doi.org/10.1088/0004-637X/702/2/1353)
- Diaz, Y., Hernández-García, L., Arévalo, P., et al. 2023, *A&A*, 669, A114, doi: [10.1051/0004-6361/202244678](https://doi.org/10.1051/0004-6361/202244678)
- Elvis, M., Maccacaro, T., Wilson, A. S., et al. 1978, *MNRAS*, 183, 129, doi: [10.1093/mnras/183.2.129](https://doi.org/10.1093/mnras/183.2.129)
- Ezhikode, S. H., Dewangan, G. C., Misra, R., & Philip, N. S. 2020, *MNRAS*, 495, 3373, doi: [10.1093/mnras/staa1288](https://doi.org/10.1093/mnras/staa1288)
- Fabian, A. C., Lohfink, A., Kara, E., et al. 2015, *MNRAS*, 451, 4375, doi: [10.1093/mnras/stv1218](https://doi.org/10.1093/mnras/stv1218)
- Feigelson, E. D., & Nelson, P. I. 1985, *ApJ*, 293, 192, doi: [10.1086/163225](https://doi.org/10.1086/163225)
- García, J., & Kallman, T. R. 2010, *ApJ*, 718, 695, doi: [10.1088/0004-637X/718/2/695](https://doi.org/10.1088/0004-637X/718/2/695)
- García, J., Kallman, T. R., & Mushotzky, R. F. 2011, *The Astrophysical Journal*, 731, 131, doi: [10.1088/0004-637x/731/2/131](https://doi.org/10.1088/0004-637x/731/2/131)
- Guilbert, P. W., Fabian, A. C., & Rees, M. J. 1983, *MNRAS*, 205, 593, doi: [10.1093/mnras/205.3.593](https://doi.org/10.1093/mnras/205.3.593)
- Haardt, F., & Maraschi, L. 1991, *ApJL*, 380, L51, doi: [10.1086/186171](https://doi.org/10.1086/186171)
- . 1993, *ApJ*, 413, 507, doi: [10.1086/173020](https://doi.org/10.1086/173020)
- Harrison, F. A., Craig, W. W., Christensen, F. E., et al. 2013, *ApJ*, 770, 103, doi: [10.1088/0004-637X/770/2/103](https://doi.org/10.1088/0004-637X/770/2/103)
- Hinkle, J. T., & Mushotzky, R. 2021, *MNRAS*, 506, 4960, doi: [10.1093/mnras/stab1976](https://doi.org/10.1093/mnras/stab1976)
- Ho, L. C. 2008, *ARA&A*, 46, 475, doi: [10.1146/annurev.astro.45.051806.110546](https://doi.org/10.1146/annurev.astro.45.051806.110546)
- Jin, C., Ward, M., & Done, C. 2012, *MNRAS*, 425, 907, doi: [10.1111/j.1365-2966.2012.21272.x](https://doi.org/10.1111/j.1365-2966.2012.21272.x)
- Johnson, W. N., McNaron-Brown, K., Kurfess, J. D., et al. 1997, *ApJ*, 482, 173, doi: [10.1086/304148](https://doi.org/10.1086/304148)
- Kamraj, N., Harrison, F. A., Baloković, M., Lohfink, A., & Brightman, M. 2018, *ApJ*, 866, 124, doi: [10.3847/1538-4357/aadd0d](https://doi.org/10.3847/1538-4357/aadd0d)
- Kamraj, N., Brightman, M., Harrison, F. A., et al. 2022, *ApJ*, 927, 42, doi: [10.3847/1538-4357/ac45f6](https://doi.org/10.3847/1538-4357/ac45f6)
- Kang, J., Wang, J., & Kang, W. 2020, *The Astrophysical Journal*, 901, 111, doi: [10.3847/1538-4357/abaf5](https://doi.org/10.3847/1538-4357/abaf5)
- Kang, J.-L., & Wang, J.-X. 2022, *The Astrophysical Journal*, 929, 141, doi: [10.3847/1538-4357/ac5d49](https://doi.org/10.3847/1538-4357/ac5d49)
- Kang, J.-L., Wang, J.-X., & Kang, W.-Y. 2021, *MNRAS*, 502, 80, doi: [10.1093/mnras/stab039](https://doi.org/10.1093/mnras/stab039)
- Kara, E., García, J. A., Lohfink, A., et al. 2017, *MNRAS*, 468, 3489, doi: [10.1093/mnras/stx792](https://doi.org/10.1093/mnras/stx792)
- Keek, L., & Ballantyne, D. R. 2016, *MNRAS*, 456, 2722, doi: [10.1093/mnras/stv2882](https://doi.org/10.1093/mnras/stv2882)
- Liu, H., Luo, B., Brandt, W. N., et al. 2021, *ApJ*, 910, 103, doi: [10.3847/1538-4357/abe37f](https://doi.org/10.3847/1538-4357/abe37f)
- Liu, T., Wang, J.-X., Yang, H., Zhu, F.-F., & Zhou, Y.-Y. 2014, *ApJ*, 783, 106, doi: [10.1088/0004-637X/783/2/106](https://doi.org/10.1088/0004-637X/783/2/106)
- Lubiński, P., Zdziarski, A. A., Walter, R., et al. 2010, *MNRAS*, 408, 1851, doi: [10.1111/j.1365-2966.2010.17251.x](https://doi.org/10.1111/j.1365-2966.2010.17251.x)
- Lubiński, P., Beckmann, V., Gibaud, L., et al. 2016, *MNRAS*, 458, 2454, doi: [10.1093/mnras/stw454](https://doi.org/10.1093/mnras/stw454)
- Lynden-Bell, D. 1969, *Nature*, 223, 690, doi: [10.1038/223690a0](https://doi.org/10.1038/223690a0)
- Malizia, A., Molina, M., Bassani, L., et al. 2014, *ApJL*, 782, L25, doi: [10.1088/2041-8205/782/2/L25](https://doi.org/10.1088/2041-8205/782/2/L25)
- Malkan, M. A., & Sargent, W. L. W. 1982, *ApJ*, 254, 22, doi: [10.1086/159701](https://doi.org/10.1086/159701)
- Malzac, J., Beloborodov, A. M., & Poutanen, J. 2001, *MNRAS*, 326, 417, doi: [10.1046/j.1365-8711.2001.04450.x](https://doi.org/10.1046/j.1365-8711.2001.04450.x)
- Marchesi, S., Ajello, M., Marcotulli, L., et al. 2018, *ApJ*, 854, 49, doi: [10.3847/1538-4357/aaa410](https://doi.org/10.3847/1538-4357/aaa410)
- Mattson, B. J., Weaver, K. A., & Reynolds, C. S. 2007, *The Astrophysical Journal*, 664, 101, doi: [10.1086/518783](https://doi.org/10.1086/518783)
- McHardy, I. M., Gunn, K. F., Uttley, P., & Goad, M. R. 2005, *MNRAS*, 359, 1469, doi: [10.1111/j.1365-2966.2005.08992.x](https://doi.org/10.1111/j.1365-2966.2005.08992.x)
- Mejía-Restrepo, J. E., Trakhtenbrot, B., Koss, M. J., et al. 2022, *ApJS*, 261, 5, doi: [10.3847/1538-4365/ac660210.48550/arXiv.2204.05321](https://doi.org/10.3847/1538-4365/ac660210.48550/arXiv.2204.05321)
- Middei, R., Bianchi, S., Marinucci, A., et al. 2019, *A&A*, 630, A131, doi: [10.1051/0004-6361/201935881](https://doi.org/10.1051/0004-6361/201935881)
- Molina, M., Bassani, L., Malizia, A., et al. 2013, *MNRAS*, 433, 1687, doi: [10.1093/mnras/stt844](https://doi.org/10.1093/mnras/stt844)
- Molina, M., Malizia, A., Bassani, L., et al. 2019, *MNRAS*, 484, 2735, doi: [10.1093/mnras/stz156](https://doi.org/10.1093/mnras/stz156)
- Molina, M., Bassani, L., Malizia, A., et al. 2009, *MNRAS*, 399, 1293, doi: [10.1111/j.1365-2966.2009.15257.x](https://doi.org/10.1111/j.1365-2966.2009.15257.x)

- Moro, A. D., Alexander, D. M., Aird, J. A., et al. 2017, *The Astrophysical Journal*, 849, 57, doi: [10.3847/1538-4357/aa9115](https://doi.org/10.3847/1538-4357/aa9115)
- Muchotrzeb, B., & Paczynski, B. 1982, *AcA*, 32, 1
- Mushotzky, R. F., Done, C., & Pounds, K. A. 1993, *ARA&A*, 31, 717, doi: [10.1146/annurev.aa.31.090193.003441](https://doi.org/10.1146/annurev.aa.31.090193.003441)
- Nicastro, F., Piro, L., De Rosa, A., et al. 2000, *ApJ*, 536, 718, doi: [10.1086/308950](https://doi.org/10.1086/308950)
- Oh, K., Koss, M., Markwardt, C. B., et al. 2018, *The Astrophysical Journal Supplement Series*, 235, 4, doi: [10.3847/1538-4365/aaa7fd](https://doi.org/10.3847/1538-4365/aaa7fd)
- Paczynski, B., & Bisnovatyi-Kogan, G. 1981, *AcA*, 31, 283
- Pal, I., & Stalin, C. S. 2023, *MNRAS*, 518, 2529, doi: [10.1093/mnras/stac3254](https://doi.org/10.1093/mnras/stac3254)
- Pal, I., Stalin, C. S., Mallick, L., & Rani, P. 2022, *A&A*, 662, A78, doi: [10.1051/0004-6361/202142386](https://doi.org/10.1051/0004-6361/202142386)
- Panagiotou, C., & Walter, R. 2020, *A&A*, 640, A31, doi: [10.1051/0004-6361/201937390](https://doi.org/10.1051/0004-6361/201937390)
- Panagiotou, C., & Walter, R. 2019, *A&A*, 626, A40, doi: [10.1051/0004-6361/201935052](https://doi.org/10.1051/0004-6361/201935052)
- Parker, M. L., Komossa, S., Kollatschny, W., et al. 2016, *MNRAS*, 461, 1927, doi: [10.1093/mnras/stw1449](https://doi.org/10.1093/mnras/stw1449)
- Perola, G. C., Matt, G., Cappi, M., et al. 2002, *A&A*, 389, 802, doi: [10.1051/0004-6361:20020658](https://doi.org/10.1051/0004-6361:20020658)
- Petrucci, P. O., Haardt, F., Maraschi, L., et al. 2001, *ApJ*, 556, 716, doi: [10.1086/321629](https://doi.org/10.1086/321629)
- Porquet, D., Reeves, J. N., Grosso, N., Braito, V., & Lobban, A. 2021, *A&A*, 654, A89, doi: [10.1051/0004-6361/202141577](https://doi.org/10.1051/0004-6361/202141577)
- Rani, P., Stalin, C. S., & Goswami, K. D. 2019, *MNRAS*, 484, 5113, doi: [10.1093/mnras/stz275](https://doi.org/10.1093/mnras/stz275)
- Ricci, C., & Trakhtenbrot, B. 2022, arXiv e-prints, arXiv:2211.05132, doi: [10.48550/arXiv.2211.05132](https://doi.org/10.48550/arXiv.2211.05132)
- Ricci, C., Trakhtenbrot, B., Koss, M. J., et al. 2017, *The Astrophysical Journal Supplement Series*, 233, 17, doi: [10.3847/1538-4365/aa96ad](https://doi.org/10.3847/1538-4365/aa96ad)
- Ricci, C., Ho, L. C., Fabian, A. C., et al. 2018, *MNRAS*, 480, 1819, doi: [10.1093/mnras/sty1879](https://doi.org/10.1093/mnras/sty1879)
- Risaliti, G., Elvis, M., Fabbiano, G., Baldi, A., & Zezas, A. 2005, *The Astrophysical Journal*, 623, L93, doi: [10.1086/430252](https://doi.org/10.1086/430252)
- Risaliti, G., Young, M., & Elvis, M. 2009, *ApJL*, 700, L6, doi: [10.1088/0004-637X/700/1/L6](https://doi.org/10.1088/0004-637X/700/1/L6)
- Salpeter, E. E. 1964, *ApJ*, 140, 796, doi: [10.1086/147973](https://doi.org/10.1086/147973)
- Shakura, N. I., & Sunyaev, R. A. 1973, *A&A*, 24, 337
- Shemmer, O., Brandt, W. N., Netzer, H., Maiolino, R., & Kaspi, S. 2006, *ApJL*, 646, L29, doi: [10.1086/506911](https://doi.org/10.1086/506911)
- . 2008, *ApJ*, 682, 81, doi: [10.1086/588776](https://doi.org/10.1086/588776)
- Shields, G. A. 1978, *Nature*, 272, 706, doi: [10.1038/272706a0](https://doi.org/10.1038/272706a0)
- Sun, W.-H., & Malkan, M. A. 1989, *ApJ*, 346, 68, doi: [10.1086/167986](https://doi.org/10.1086/167986)
- Sunyaev, R. A., & Titarchuk, L. G. 1980, *A&A*, 86, 121
- Tazaki, F., Ueda, Y., Terashima, Y., & Mushotzky, R. F. 2011, *ApJ*, 738, 70, doi: [10.1088/0004-637X/738/1/70](https://doi.org/10.1088/0004-637X/738/1/70)
- Thorne, K. S. 1974, *ApJ*, 191, 507, doi: [10.1086/152991](https://doi.org/10.1086/152991)
- Tortosa, A., Ricci, C., Ho, L. C., et al. 2022a, arXiv e-prints, arXiv:2212.06183, <https://arxiv.org/abs/2212.06183>
- Tortosa, A., Ricci, C., Tombesi, F., et al. 2022b, *MNRAS*, 509, 3599, doi: [10.1093/mnras/stab3152](https://doi.org/10.1093/mnras/stab3152)
- Tortosa, A., Bianchi, S., Marinucci, A., Matt, G., & Petrucci, P. O. 2018, *A&A*, 614, A37, doi: [10.1051/0004-6361/201732382](https://doi.org/10.1051/0004-6361/201732382)
- Trakhtenbrot, B., Ricci, C., Koss, M. J., et al. 2017, *MNRAS*, 470, 800, doi: [10.1093/mnras/stx1117](https://doi.org/10.1093/mnras/stx1117)
- Turner, T. J., Reeves, J. N., Braito, V., & Costa, M. 2018, *MNRAS*, 476, 1258, doi: [10.1093/mnras/sty318](https://doi.org/10.1093/mnras/sty318)
- Ursini, F., Petrucci, P. O., Matt, G., et al. 2016, *MNRAS*, 463, 382, doi: [10.1093/mnras/stw2022](https://doi.org/10.1093/mnras/stw2022)
- Ursini, F., Boissay, R., Petrucci, P.-O., et al. 2015, *A&A*, 577, A38, doi: [10.1051/0004-6361/201425401](https://doi.org/10.1051/0004-6361/201425401)
- Vasudevan, R. V., & Fabian, A. C. 2007, *Monthly Notices of the Royal Astronomical Society*, 381, 1235, doi: [10.1111/j.1365-2966.2007.12328.x](https://doi.org/10.1111/j.1365-2966.2007.12328.x)
- Vasudevan, R. V., Mushotzky, R. F., & Gandhi, P. 2013, *ApJL*, 770, L37, doi: [10.1088/2041-8205/770/2/L37](https://doi.org/10.1088/2041-8205/770/2/L37)
- Wang, J. M., & Netzer, H. 2003, *A&A*, 398, 927, doi: [10.1051/0004-6361:20021511](https://doi.org/10.1051/0004-6361:20021511)
- Wang, J.-M., Du, P., Hu, C., et al. 2014, *The Astrophysical Journal*, 793, 108, doi: [10.1088/0004-637X/793/2/108](https://doi.org/10.1088/0004-637X/793/2/108)
- Willingale, R., Starling, R. L. C., Beardmore, A. P., Tanvir, N. R., & O'Brien, P. T. 2013, *MNRAS*, 431, 394, doi: [10.1093/mnras/stt175](https://doi.org/10.1093/mnras/stt175)
- Winkler, H. 1992, *MNRAS*, 257, 677, doi: [10.1093/mnras/257.4.677](https://doi.org/10.1093/mnras/257.4.677)
- Zappacosta, L., Comastri, A., Civano, F., et al. 2018, *The Astrophysical Journal*, 854, 33, doi: [10.3847/1538-4357/aaa550](https://doi.org/10.3847/1538-4357/aaa550)
- Zdziarski, A. A., Johnson, W. N., & Magdziarz, P. 1996, *MNRAS*, 283, 193, doi: [10.1093/mnras/283.1.193](https://doi.org/10.1093/mnras/283.1.193)
- Zdziarski, A. A., Lubiński, P., & Smith, D. A. 1999, *MNRAS*, 303, L11, doi: [10.1046/j.1365-8711.1999.02343.x](https://doi.org/10.1046/j.1365-8711.1999.02343.x)
- Zdziarski, A. A., Lubiński, P., Gilfanov, M., & Revnivtsev, M. 2003, *Monthly Notices of the Royal Astronomical Society*, 342, 355, doi: [10.1046/j.1365-8711.2003.06556.x](https://doi.org/10.1046/j.1365-8711.2003.06556.x)
- Zdziarski, A. A., Poutanen, J., & Johnson, W. N. 2000, *ApJ*, 542, 703, doi: [10.1086/317046](https://doi.org/10.1086/317046)

Zhang, J.-X., Wang, J.-X., & Zhu, F.-F. 2018, *ApJ*, 863, 71,
doi: [10.3847/1538-4357/aacf92](https://doi.org/10.3847/1538-4357/aacf92)
Zoghbi, A., Matt, G., Miller, J. M., et al. 2017, *ApJ*, 836, 2,
doi: [10.3847/1538-4357/aa582c](https://doi.org/10.3847/1538-4357/aa582c)

Życki, P. T., Done, C., & Smith, D. A. 1999, *MNRAS*, 309,
561, doi: [10.1046/j.1365-8711.1999.02885.x](https://doi.org/10.1046/j.1365-8711.1999.02885.x)